Original

Li, D.; Yin, B.; Feng, J.; Dosio, A.; Geyer, B.; Qi, J.; Shi, H.; Xu, Z.:
Present Climate Evaluation and Added Value Analysis of Dynamically Downscaled Simulations of CORDEX - East Asia
In: Journal of Applied Meteorology and Climatology (2018) AMS

DOI: 10.1175/JAMC-D-18-0008.1

Present Climate Evaluation and Added Value Analysis of Dynamically Downscaled Simulations of CORDEX—East Asia

DELEI LI,[a,b,c] BAOSHU YIN,[a,b,c,d] JIANLONG FENG,[e] ALESSANDRO DOSIO,[f] BEATE GEYER,[g] JIFENG QI,[a,b,c] HONGYUAN SHI,[h] AND ZHENHUA XU[a,b,c]

[a] *Key Laboratory of Ocean Circulation and Waves, Institute of Oceanology, Chinese Academy of Sciences, Qingdao, China*
[b] *Function Laboratory for Ocean Dynamics and Climate, Qingdao National Laboratory for Marine Science and Technology, Qingdao, China*
[c] *Center for Ocean Mega-Science, Chinese Academy of Sciences, Qingdao, China*
[d] *University of Chinese Academy of Sciences, Beijing, China*
[e] *National Marine Data and Information Service, Tianjin, China*
[f] *European Commission, Joint Research Centre, Ispra, Italy*
[g] *Helmholtz-Zentrum Geesthacht Centre for Materials and Coastal Research, Geesthacht, Germany*
[h] *School of Civil Engineering, Ludong University, Yantai, China*

(Manuscript received 12 January 2018, in final form 19 July 2018)

ABSTRACT

In this study, we investigate the skills of the regional climate model Consortium for Small-Scale Modeling in Climate Mode (CCLM) in reproducing historical climatic features and their added value to the driving global climate models (GCMs) of the Coordinated Regional Climate Downscaling Experiment—East Asia (CORDEX-EA) domain. An ensemble of climate simulations, with a resolution of 0.44°, was conducted by downscaling four GCMs: CNRM-CM5, EC-EARTH, HadGEM2, and MPI-ESM-LR. The CCLM outputs were compared with different observations and reanalysis datasets. Results showed strong seasonal variability of CCLM's ability in reproducing climatological means, variability, and extremes. The bias of the simulated summer temperatures is generally smaller than that of the winter temperatures; in addition, areas where CCLM adds value to the driving GCMs in simulating temperature are larger in the winter than in the summer. CCLM outperforms GCMs in terms of generating climatological precipitation means and daily precipitation distributions for most regions in the winter, but this is not always the case for the summer. It was found that CCLM biases are partly inherited from GCMs and are significantly shaped by structural biases of CCLM. Furthermore, downscaled simulations show added value in capturing features of consecutive wet days for the tropics and of consecutive dry days for areas to the north of 30°N. We found considerable uncertainty from reanalysis and observation datasets in temperatures and precipitation climatological means for some regions that rival bias values of GCMs and CCLM simulations. We recommend carefully selecting reference datasets when evaluating modeled climate means.

1. Introduction

Climatic changes have significant impacts on natural and human systems worldwide. In particular, changes in climate extremes such as heat waves, droughts, and floods associated with medium- and high-emissions scenarios for this century present high risks of abrupt and irreversible changes to terrestrial and ocean ecosystems, freshwater resources, food production, and human health (IPCC 2014a). Global climate models (GCMs) and Earth system models (ESMs) are the primary and most comprehensive tools used to simulate past and future climatic change. They have been demonstrated to capture climate variability and features at both continental and global scales (Sperber et al. 2013). However, GCMs and ESMs are less effective at simulating regional climate information because of their generally coarse resolution, which currently ranges from 100 to 200 km for the atmospheric component and approximately 100 km for the oceanic component (Bao et al. 2015). Hostetler et al. (2011), for instance, showed that global spatial patterns and gradients of air temperature can generally be

Supplemental information related to this paper is available at the Journals Online website: https://doi.org/10.1175/JAMC-D-18-0008.s1.

Corresponding author: Zhenhua Xu, xuzhenhua@qdio.ac.cn

DOI: 10.1175/JAMC-D-18-0008.1

captured by GCMs, while those of precipitation are not resolved as satisfactorily. Most GCMs tend to overestimate precipitation levels for the western region of North America while underestimating levels for the eastern region of North America. Mehran et al. (2014) validated phase 5 of the Coupled Model Intercomparison Project (CMIP5) GCMs against Global Precipitation Climatology Project (GPCP) precipitation data and concluded that CMIP5 GCMs are in good agreement with GPCP data in several areas but not for arid and certain subcontinental regions such as northern Eurasia and eastern Russia. CMIP5 GCMs generally exhibit limited ability to simulate high quartiles of precipitation and overestimate precipitation levels for regions characterized by complex topography. On the basis of a gridded observational extreme index dataset [Hadley Centre global climate extremes index 2 (HadEX2)], Sillmann et al. (2013) showed that CMIP5 GCMs are able to simulate climate extremes and related trend patterns. They also suggested using reference datasets carefully when evaluating climate model simulations in terms of extremes indices while considering significant sources of uncertainty among reference datasets.

Climate changes, especially in the case of extreme climate change, generally feature high levels of spatial and temporal variability. A better understanding of regional climate characteristics with a focus on the frequency and intensity of extreme events and related changes is of vital importance to climate risk assessments as well as adaptation implementation for regional communities. A better representation of these local specifications can typically be obtained through either empirical–statistical downscaling or dynamical downscaling. The latter generally uses regional climate models (RCMs) driven by GCM output or reanalysis data to derive regional climate information. Regional climate modeling was pioneered by Giorgi and Bates (1989) and has been widely used in climate change and extreme climate event studies conducted at regional and local scales. From high spatial resolutions of limited areas, RCMs can capture physiographic features such as coastlines, mountains, and surface characteristics in great detail and can consequently reproduce finescale atmospheric processes and features and especially for regions along coasts and with complex topographical characteristics (Feser et al. 2011; Li et al. 2016; Li 2017; von Storch et al. 2017).

East Asia is one of the most vulnerable regions to climate change because of its various terrestrial features, complex climate system, and very high population density. The region is greatly influenced by monsoon systems, which are typically accompanied by the occurrence of extreme events such as tropical cyclones, floods, and droughts. In past years, several studies have been conducted on the climate changes over East Asia based on observations or models (Liu et al. 1994; Gao et al. 2002; Fu et al. 2005; Zhang et al. 2009; Kusunoki et al. 2011; Zou and Zhou 2013; Ji and Kang 2015; Kumar et al. 2015; Wu et al. 2016; Zou et al. 2016; Zhou et al. 2016; Um et al. 2017; Xie et al. 2017). Observation results reveal that mean annual temperatures and heat wave frequencies for most regions of East Asia have increased since the middle of the twentieth century, while precipitation trends, including those of extreme precipitation, show strong levels of spatial variability (IPCC 2014b). Studies have indicated that CMIP5 GCMs can satisfactorily reproduce spatial patterns and interannual variability in surface temperatures for China, while this is not the case for precipitation (Guo et al. 2013; Huang et al. 2013; Chen and Frauenfeld 2014). Lee and Hong (2014) revealed that increasing the spatial resolution of the RCM improves simulated precipitation and temperature results and extreme event features for the Korean Peninsula. They also found that the added value of an RCM is more evident for precipitation patterns than for temperature patterns. However, Ji and Kang (2015) found that regional climate model RegCM4 simulates temperature extremes more accurately than precipitation.

In recent decades, many climate studies based on dynamical downscaling for East Asia have been conducted based on the framework of the Regional Climate Model Intercomparison Project (RMIP) for Asia to improve our understanding of climatic patterns of the East Asian monsoon region and to provide reliable regional climate scenarios (Fu et al. 2005; Niu et al. 2015; Tang et al. 2016; Wu et al. 2016). Niu et al. (2015) found that RCMs outperform the driving GCM in reproducing the summer mean precipitation distribution and annual cycle for China, while deficiencies in simulating summer precipitation are mainly attributed to limited capacities to reproduce low-level circulation. Wu et al. (2016) showed that the RCM ensemble mean is superior in reproducing both total and extreme summer precipitation relative to each individual RCM.

Recently, a globally coordinated downscaling framework called the Coordinated Regional Downscaling Experiment (CORDEX; Giorgi et al. 2009), an initiative of the World Climate Research Programme (WCRP 2009), was established to further advance RCM development, evaluation, analysis, and application. Ensembles of dynamical or statistical models driven by multiple CMIP5 GCMs have been created or are currently under way for multiple regions throughout the world (http://www.cordex.org/domains/). Within the CORDEX—East Asia domain (CORDEX-EA), several efforts have been undertaken to study mean climates and extreme changes under the

international CORDEX framework (Wang et al. 2013; Lee et al. 2014; Oh et al. 2014; Huang et al. 2015; Zou et al. 2016; Park et al. 2016).

Huang et al. (2015) showed that the ensemble mean of RCMs can reasonably simulate seasonal means, annual cycles, and interannual variability in precipitation, while individual RCMs generate significant biases for some subregions and seasons. Zou et al. (2016) showed that a regional ocean–atmosphere coupled model outperforms an uncoupled RCM in simulating spatial patterns of low-level monsoon flows crossing East Asia and the western North Pacific. Park et al. (2016) evaluated the performance of multiple RCMs in simulating summer climate extremes of the CORDEX-EA and demonstrated that RCMs present systematic biases in both seasonal means and extremes of air temperature and precipitation. Their inter-RCM analysis reveals a close relationship between model capacities to determine means and extreme values.

Previous studies have revealed the importance of multimodel ensembles in modeling regional climate statistics and climate change. However, many studies have been based on either a single GCM or RCM model (Brown et al. 2010; Gao et al. 2012a) or on several RCMs driven by the same GCM of CMIP3 (e.g., Niu et al. 2015; Um et al. 2017; Wu et al. 2016). Furthermore, most studies have used only one observation dataset for reference without considering uncertainties among observation datasets. Considerable uncertainties found among observation products have been revealed by many studies of the global landmass (e.g., Fekete et al. 2004) and of specific regions (e.g., Xie et al. 2007). The effects of these uncertainties on the assessment of model performance must be seriously considered.

In this study, the performance of the RCM known as Consortium for Small-Scale Modeling in Climate Mode (CCLM) driven by various CMIP5 GCMs was evaluated against several temperature and precipitation observation or reanalysis datasets. Uncertainties generated from the use of different driving GCMs together with the added value of dynamical downscaling were assessed for the present period for both mean climate and extreme values. The influence of observation uncertainties on model performance is discussed as well.

The paper is organized as follows: Section 2 describes the experimental setups and datasets used. Section 3 presents our evaluation results of model performance in simulating seasonal mean air temperatures, climatology, and variability of precipitation as well as large-scale circulation. Section 4 describes the capacity to which CCLM can simulate extreme precipitation patterns. Section 5 presents a summary and concluding remarks.

2. Experimental setups and datasets

a. Model description and simulation setups

Version 5.0 of the nonhydrostatic CCLM (also called the COSMO-CLM; Rockel et al. 2008) RCM is used in this study. It is the climate version of the operational weather forecast model COSMO, which was developed by the German Weather Service (DWD). The model is based on Navier–Stokes primitive equations that describe nonhydrostatic compressible flows in a moist atmosphere. The equations are solved on an Arakawa C grid within a rotated geographical coordinate system and with a generalized terrain-following height coordinate (Schättler et al. 2018).

CCLM has been used in climate studies for many regions worldwide (Rockel and Geyer 2008). It has been used in several international projects [e.g., the Prediction of Regional Scenarios and Uncertainties for Defining European Climate Change Risks and Effects (PRUDENCE; Christensen et al. 2007), "ENSEMBLES" (van der Linden and Mitchell 2009), and the European branch of the World Climate Research Program Coordinated Regional Downscaling Experiment (EURO-CORDEX; Jacob et al. 2014) of the Global Energy and Water Cycle Experiment (GEWEX; https://www.gewex.org/) and its successor CORDEX (Giorgi et al. 2009)].

In this study, the model domain of CCLM is set to the CORDEX region 7 or East Asia domain (Fig. 1) among CORDEX initiatives (Giorgi et al. 2009). The horizontal resolution is set to 0.44° with 223 × 187 grid points established in the longitudinal and latitudinal directions, respectively. The temporal integration of the simulations is carried out using the Runge–Kutta scheme with a time step of 300 s. Ten grid boxes are set as a sponge zone at each lateral boundary. Given the substantial extension of troposphere height across the tropical region, we set the lower boundary of the Rayleigh damping layer in the model at 18 km rather than at the typical value of 11 km to avoid generating unrealistic results (Dosio et al. 2015). There are 45 vertical levels, with the top of the model domain at 30 000 m in height.

Regional climate simulations of the CORDEX-EA were conducted for the current climate period of 1950–2005 by downscaling from four CMIP5 GCMs (see Table 1): CNRM-CM5 (Voldoire et al. 2013), EC-EARTH (Hazeleger et al. 2010), HadGEM2 (Collins et al. 2011), and MPI-ESM-LR (Giorgetta et al. 2012). According to McSweeney et al. (2015), CNRM-CM5, HadGEM2, and MPI-ESM-LR are suitable GCMs for generating downscaled climate for three subregions, that is, Southeast Asia, Europe, and Africa. The performance

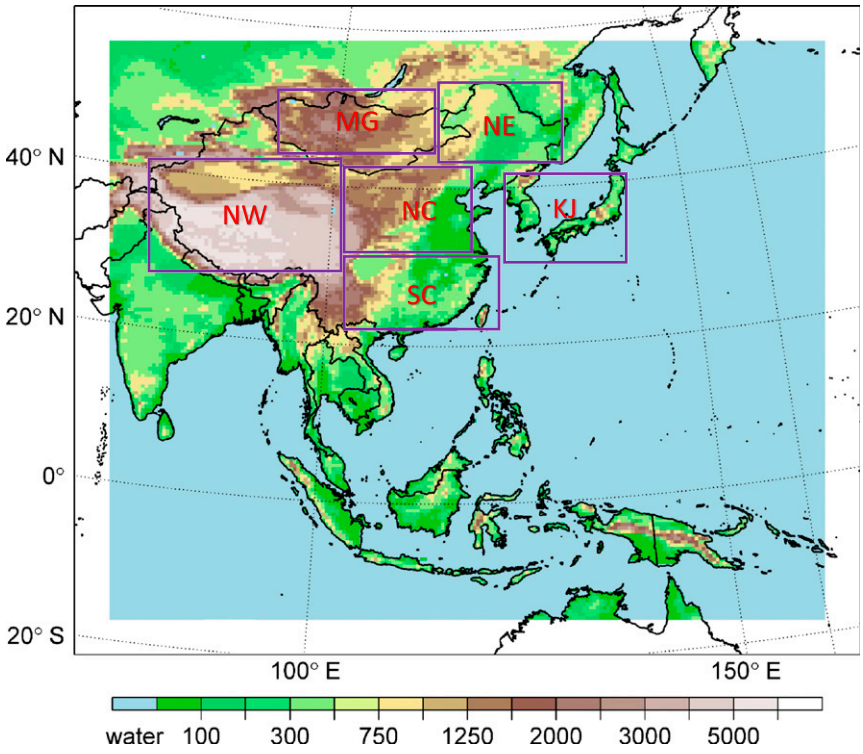

FIG. 1. Model domain and orography of the CORDEX-EA simulations. The six subregions are western China (WC), Mongolia (MG), southern China (SC), northern China (NC), northeastern China (NE), and the Korean Peninsula and Japan (KJ). The white frame indicates the sponge zone.

of EC-EARTH, although not as satisfactory, is considered to be acceptable in representing regional large-scale circulation and annual cycling features of temperature and precipitation.

Various physical parameterization schemes (Table 2, left column) were used in the simulations, including the Tiedtke mass-flux convection scheme (Tiedtke 1989), the prognostic turbulent kinetic energy closure scheme, multilayer land surface scheme "TERRA-ML" for land surface processes (Schrodin and Heise 2002), and the radiation scheme with full cloud radiation (Ritter and Geleyn 1992). The preprocessor (PEP) tool of the CCLM software package was used to generate invariant external forcing data (Table 2, right column) such as surface height, roughness length, and soil.

b. *Datasets and statistical indices*

In considering the uncertainties of the reference datasets and their effects on model performance, three of the latest reanalysis datasets and five observation datasets (Table 3) were used to evaluate the quality of the CCLM results and to assess their added values to the forcing GCMs. For the precipitation evaluations, GPCP (Huffman et al. 2001), Global Precipitation Climatology Centre (GPCC; Schneider et al. 2014), Tropical Rainfall Measuring Mission (TRMM; Huffman et al. 2007), Asian Precipitation—Highly Resolved Observational Data Integration Towards Evaluation of Water Resources (APHRODITE; Yatagai et al. 2012), and Climatic Research Unit (CRU; Harris et al. 2014) data were used. The CRU, ERA-Interim reanalysis (ERAI; Dee et al. 2011),

TABLE 1. Information on the four GCMs used in this analysis.

Model	Institution/country	Grids	Vertical levels
CNRM-CM5	National Centre for Meteorological Research, France	256 × 128	31
EC-EARTH	EC-EARTH Consortium, Europe	320 × 160	62
HadGEM2(-ES)	Met Office Hadley Centre, United Kingdom	360 × 181	38
MPI-ESM-LR	Max Planck Institute for Meteorology, Germany	192 × 96	47

TABLE 2. Basic configuration schemes and invariant external forcings of the CCLM simulations.

Physical parameterization schemes	Invariant external forcings
Convection scheme: Tiedtke (1989)	Orography: Global Land One-km Base Elevation (GLOBE) (NOAA/NGDC)
Time-integration scheme: Runge–Kutta	Surface roughness: GLOBE (NOAA/NGDC); Global Land Cover 2000 Project (GLC2000) [Joint Research Centre (JRC) Ispra]
Turbulence scheme: Prognostic turbulent kinetic energy closure	Land–sea fraction, parameters of vegetation, leaf area, and root depth: GLC2000 (JRC Ispra)
Radiation scheme: Ritter and Geleyn (1992)	Near surface temperature: CRU (University of East Anglia)
Microphysics scheme: Kessler type (Kessler 1969)	Soil type: Digital Soil Map of the World (Food and Agriculture Organization of the United Nations)
Land surface processes: Multilayer soil model TERRA-ML (Schrodin and Heise 2002)	Surface albedo: MODIS soil color derived soil albedo (NASA)
Subgrid-scale orography scheme: Lott and Miller (1997); Schulz (2008)	Aerosol optical thickness: NASA/GISS (Global Aerosol Climatology Project)

Japanese 55-yr Reanalysis (JRA-55; Kobayashi et al. 2015), and Modern-Era Retrospective Analysis for Research and Applications, version 2, reanalysis (MERRA-2; Gelaro et al. 2017) datasets were used for temperature evaluations.

To draw comparisons, coarse-resolution GCMs, reanalysis datasets and observation datasets were interpolated to the CCLM grid (0.44° resolution) via bilinear interpolation. Periods of available observations vary among the datasets, and the period for each dataset is given in Table 3. Note that the CORDEX-EA region is not fully covered by the TRMM precipitation dataset. The following statistical results related to the TRMM precipitation dataset are limited to the region covering 50°S to 50°N.

To investigate spatial variations in model performance, several land subregions (shown in Fig. 1) are defined for the CORDEX-EA domain following Zou et al. (2016). To assess model performance in reproducing climatological patterns and temperature and precipitation extremes, several statistics are used, including the climatological mean (MEAN), mean bias (BIAS), spatial correlation (CORR), standard deviation error (STDE), and added value index (AVI). Here, the STDE is defined as variability in the error around its mean (see von Storch and Zwiers 1999) and is written as

$$\mathrm{STDE} = (\mathrm{RMSE}^2 - \mathrm{BIAS}^2)^{1/2} = \left\{ \frac{1}{N}\sum_{i=1}^{N}(x_i')^2 - \left[\frac{1}{N}\sum_{i=1}^{N}(x_i')\right]^2 \right\}^{1/2},$$

where N denotes the number of valid pairs of simulated and observed variables determined spatially and x_i' is the deviation between counterparts of the simulated and observed variable.

AVI is defined following Dosio et al. (2015) as

$$\mathrm{AVI} = \frac{(X_{\mathrm{GCM}} - X_{\mathrm{OBS}})^2 - (X_{\mathrm{CCLM}} - X_{\mathrm{OBS}})^2}{\max\left[(X_{\mathrm{GCM}} - X_{\mathrm{OBS}})^2, (X_{\mathrm{CCLM}} - X_{\mathrm{OBS}})^2\right]},$$

where X_A denotes the seasonally averaged variable of dataset A. The AVI value ranges from −1 to 1: a positive AVI, when the squared error of the CCLM

TABLE 3. Reference datasets for model evaluation.

Dataset	Variable used	Comparison period	Temporal resolution	Spatial resolution (coverage)	Reference
GPCP v1.2	Precipitation	Dec 1996–Nov 2005	Daily	1° (global)	Huffman et al. (2001)
GPCC v7	Precipitation	Dec 1979–Nov 2005	Monthly	0.5° (global land)	Schneider et al. (2014)
TRMM 3B42	Precipitation	Jan 1998–Dec 2005	Daily	0.25° (50°S–50°N)	Huffman et al. (2007)
APHRODITE	Precipitation	Dec 1979–Nov 2005	Monthly	0.5° (Asian land)	Yatagai et al. (2012)
CRU v4.0	Precipitation; temperature	Dec 1979–Nov 2005	Monthly	0.5° (global land)	Harris et al. (2014)
ERAI	Temperature	Dec 1979–Nov 2005	Monthly	0.75° (global)	Dee et al. (2011)
JRA-55	Temperature	Dec 1979–Nov 2005	Monthly	0.5625° (global)	Kobayashi et al. (2015)
MERRA-2	Temperature	Dec 1979–Nov 2005	Monthly	0.625° (global)	Gelaro et al. (2017)

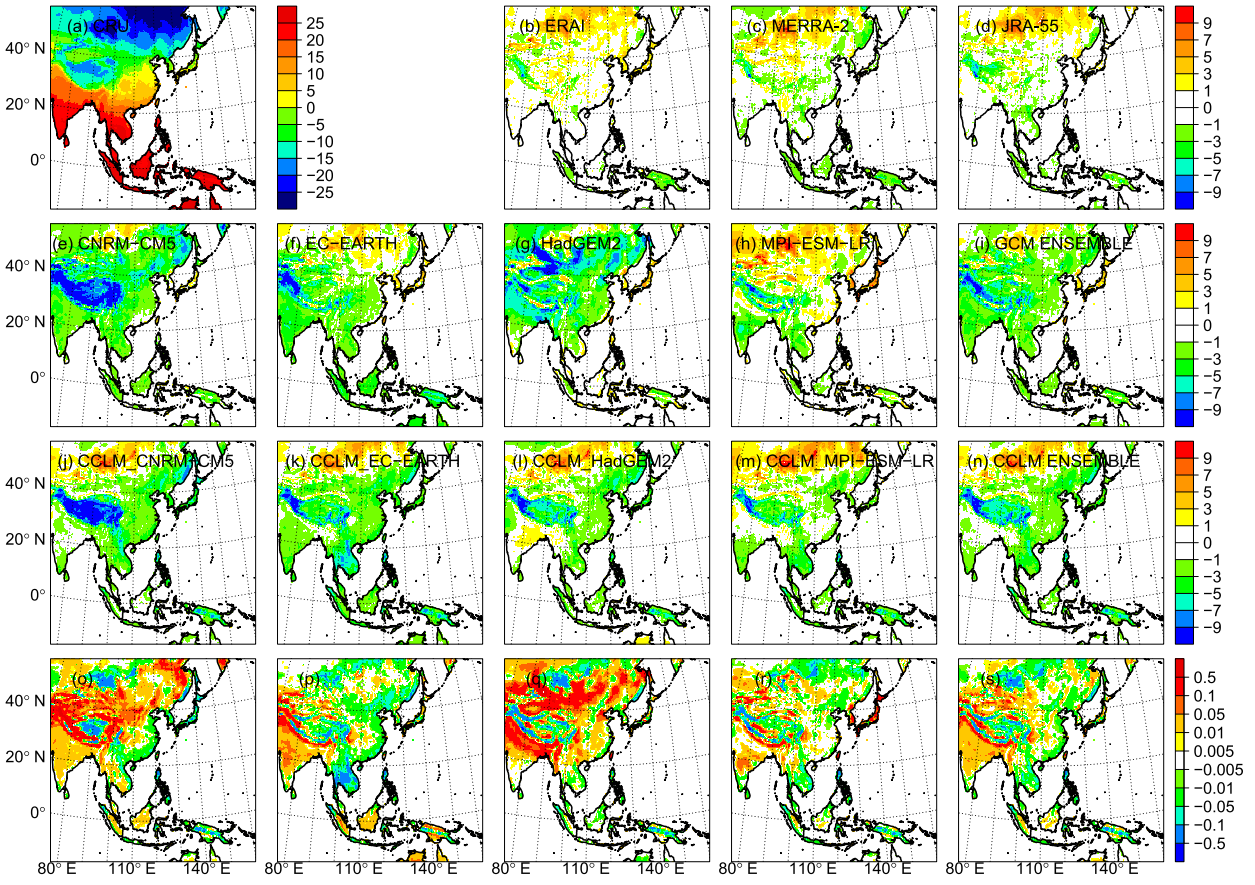

FIG. 2. (a) Observed seasonal mean temperature (°C) from CRU for DJF for December 1979–November 2005. (b)–(d) Biases of the other reanalysis datasets against CRU. (e)–(n) Biases of the GCMs, CCLM simulations, and ensemble means against CRU. (o)–(s) Added value index of seasonal mean temperatures for each GCM–CCLM combination.

dataset is smaller than that of the GCM dataset, denotes an added value from dynamical downscaling, and vice versa.

3. Mean climatology and the added value of dynamical downscaling

In this section, we thoroughly assess the capacity of CCLM to reproduce principal features of East Asian climatology for the summer [June–August (JJA)] and winter [December–February (DJF)]. We first evaluate the quality and added value of mean downscaled 2-m temperature and precipitation with respect to forcing GCMs by means of a spatial and temporal statistical analysis. Second, the performance of CCLM in representing precipitation climate features is analyzed in detail in terms of annual cycles and intensity distributions. We also compare different observation (reanalysis) datasets against the reference dataset to quantify uncertainties in observations and their potential influence on the assessment of model performance. Finally, we quantify the capacity of CCLM to resolve low-level circulation and its influence on the modeling of precipitation.

a. Temperature climatology

Figures 2 and 3 show the spatial distributions of mean biases of modeled 2-m temperature for the winter and summer and the added value index for the period December 1979–November 2005. The reanalysis datasets (Figs. 2b–d) present significantly positive winter temperature biases (3°–7°C) for Mongolia (MG) and part of northeastern China (NE). For the other regions, biases mostly range from −3° to 3°C. Winter 2-m temperatures are generally underestimated relative to CRU values for three of four GCMs (Figs. 2e–h) and to up to 5°C for most regions such as southern China (SC), western China (WC), India, the Indo-China Peninsula, and the "Maritime Continent." This underestimation can reach very large values (9°C) for the Tibetan Plateau and especially when using CNRM-CM5 (Fig. 2e). In contrast, MPI-ESM-LR (Fig. 2h) presents strong overestimations for China and MG. All of the CCLM results

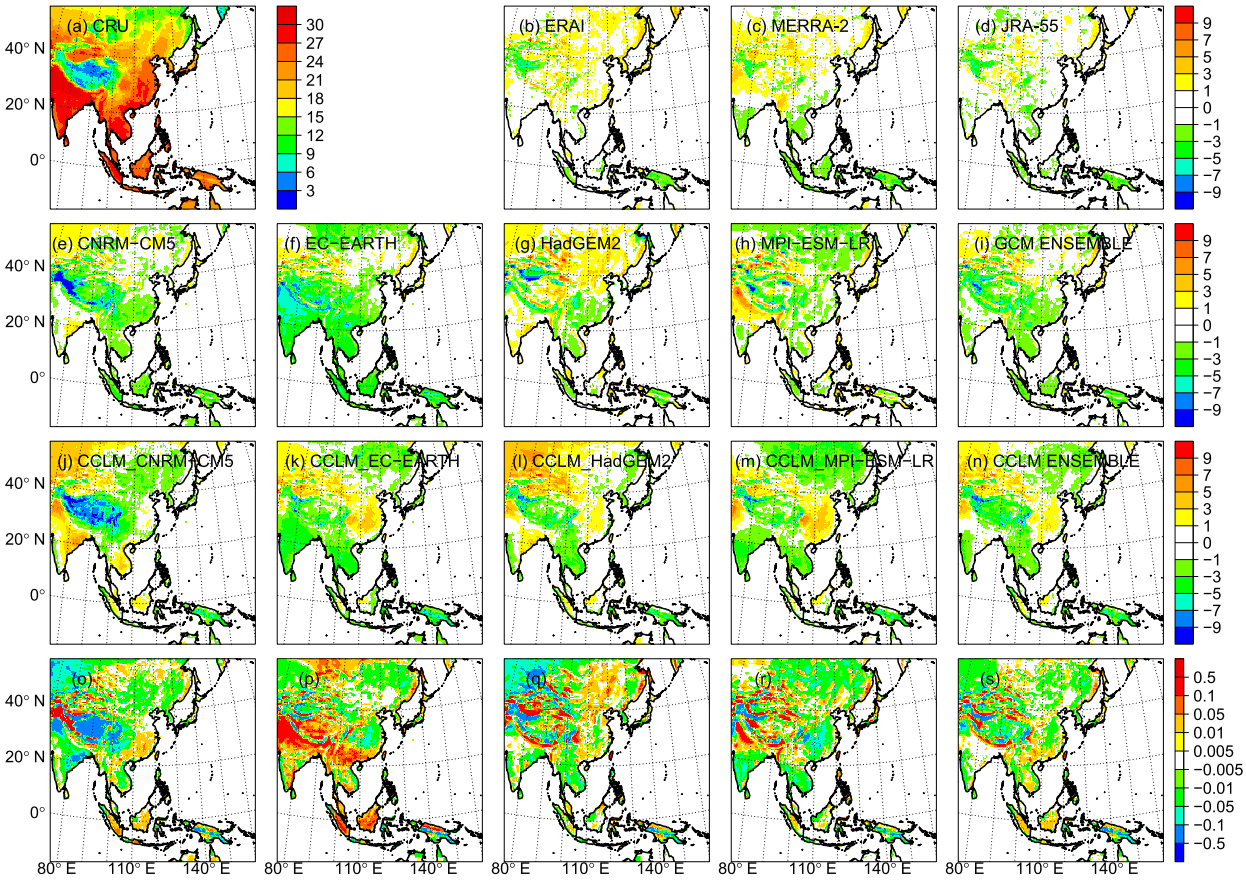

FIG. 3. As in Fig. 2, but for JJA.

(Figs. 2j–n) overestimate observed winter 2-m temperatures for MG and for part of northwestern China. Areas for which CCLM_MPI-ESM-LR (Fig. 2m) overestimates simulated temperature are larger than those shown by the other three CCLM simulations, which is consistent with their GCM counterparts.

In analyzing the geographical distribution of the added value index, for the winter (Figs. 2o–s), we note that positive AVI distributions share consistent features among simulations and mainly cover India and parts of northwestern China. The CNRM-CM5- and HadGEM2-driven simulations (Figs. 2o,q) show larger fractions of the CORDEX-EA domain with positive AVI values compared to the other two simulations. Added value distributions can also be observed from GCM and RCM ensemble-mean results (Fig. 2s). Furthermore, we note that deterioration as a result of downscaling is mainly observed for the Tibetan Plateau, for Mongolia, and for areas of coastal China for which temperature biases generated by CCLM simulations are more significant than those generated by GCMs. However, it is evident that large temperature biases of CCLM simulations for some of these regions are comparable to those of reanalysis datasets (Figs. 2b–d). Furthermore, strong negative biases observed from CCLM simulations of WC (Figs. 2j–n) mostly fall within the range of observation uncertainty (see Fig. S1e in the online supplemental material), implying acceptable simulated results by CCLM.

Model biases in 2-m mean temperatures for the summer (Fig. 3) differ considerably from those for the winter. The biases of reanalysis datasets mostly range from −3° to 3°C with a positive bias found for the East Asian continent and with a negative bias found for the Maritime Continent. Furthermore, from several observation datasets we find considerable levels of observation uncertainty for the Tibetan Plateau (see Fig. S2 in the online supplemental material). The standard deviation between observations can exceed a value of 3°C. GCMs generally show biases from −3° to 3°C; among them, HadGEM2 presents the largest fraction of the CORDEX-EA domain with a positive bias. From our CCLM simulations, we observe positive biases that are greater than corresponding GCM values for several regions. However, the bias of spatial distributions between the GCM and corresponding CCLM run is generally consistent.

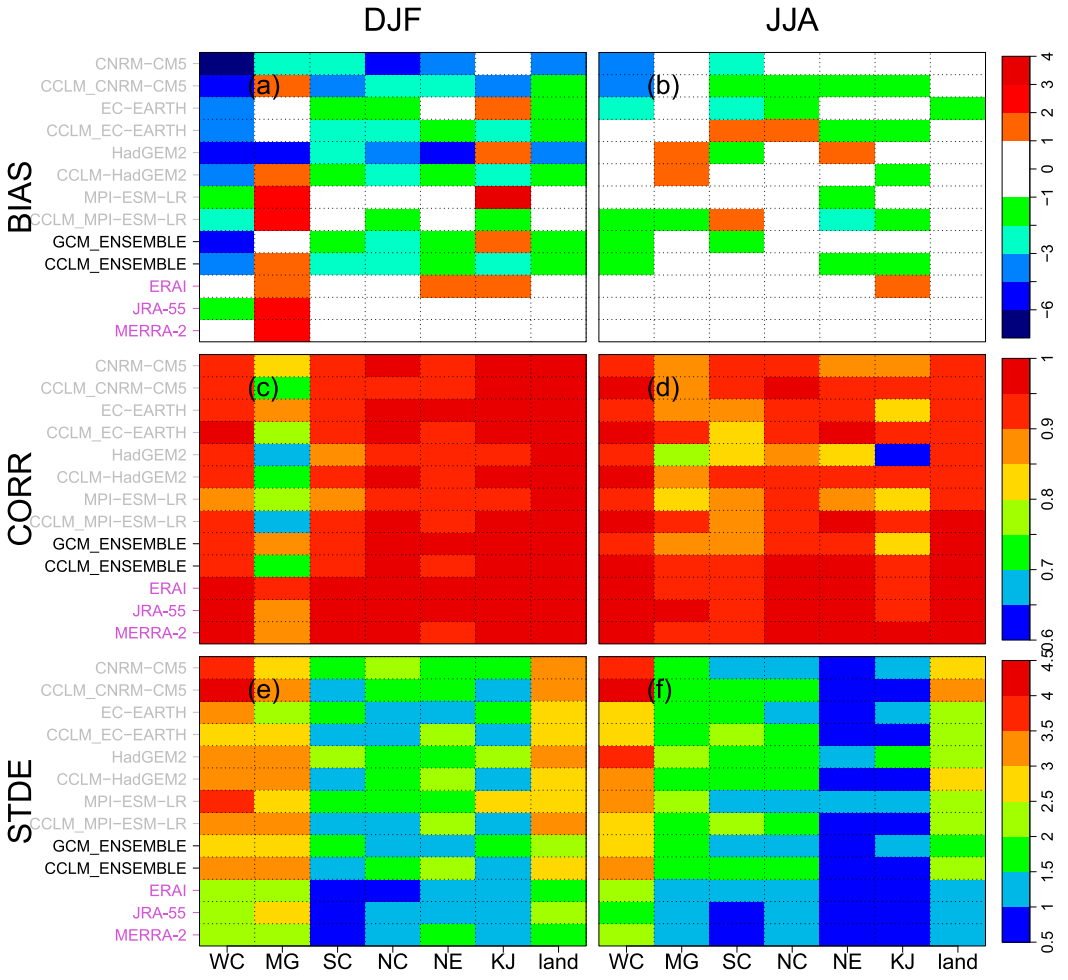

FIG. 4. Heat maps showing statistical metrics of (a), (b) regional means of bias; (c), (d) spatial correlations; and (e), (f) STDE between GCM/CCLM/reanalysis datasets and CRU surface temperature derived from (left) DJF and (right) for different subregions. "Land" denotes the mean for all land areas in the domain.

The geographical distribution of the AVI (Figs. 3o–s) is rather heterogeneous without presenting noticeably consistent patterns between different GCM–RCM combinations. Furthermore, the models' ensemble means (Figs. 3i,n,s) do not present obvious signs of added value when comparing downscaled results to those of the driving GCMs. The absolute biases of GCMs and CCLMs are generally less significant than the corresponding biases for the winter (Figs. 2i,n). A comparison of Fig. 2 and Fig. 3 reveals considerable seasonal variability in bias values and added value distributions for 2-m temperatures with less significant biases for the summer but larger areas for which the AVI is positive for the winter.

Using various statistical metrics, we further evaluate the performance of GCMs, CCLM simulations, corresponding ensemble means, and three reanalysis datasets in reproducing the 2-m temperature climatology of different land subregions and of the entire land area (i.e., all land points of the CORDEX-EA domain) for the winter and summer (Fig. 4). This analysis further confirms our findings that temperature underestimations are widely distributed for the winter but not over the MG and Korean Peninsula and Japan (KJ) for GCMs and that summer biases are much less significant than those for the winter for both GCM and CCLM runs. An area-averaged bias is found at within ±2°C for the summer for most subregions. Reanalysis datasets reveal considerably positive biases for the winter for the MG (and for the NE and KJ for the ERAI), where GCMs and CCLM simulations do not perform realistically.

In terms of spatial correlation distributions, we note that values are mostly larger than 0.9, while correlations are relatively lower for the MG region for the winter and for the KJ region for the summer. From ensemble-mean results, we find a clear improvement in spatial correlations by downscaling all subregions for the summer,

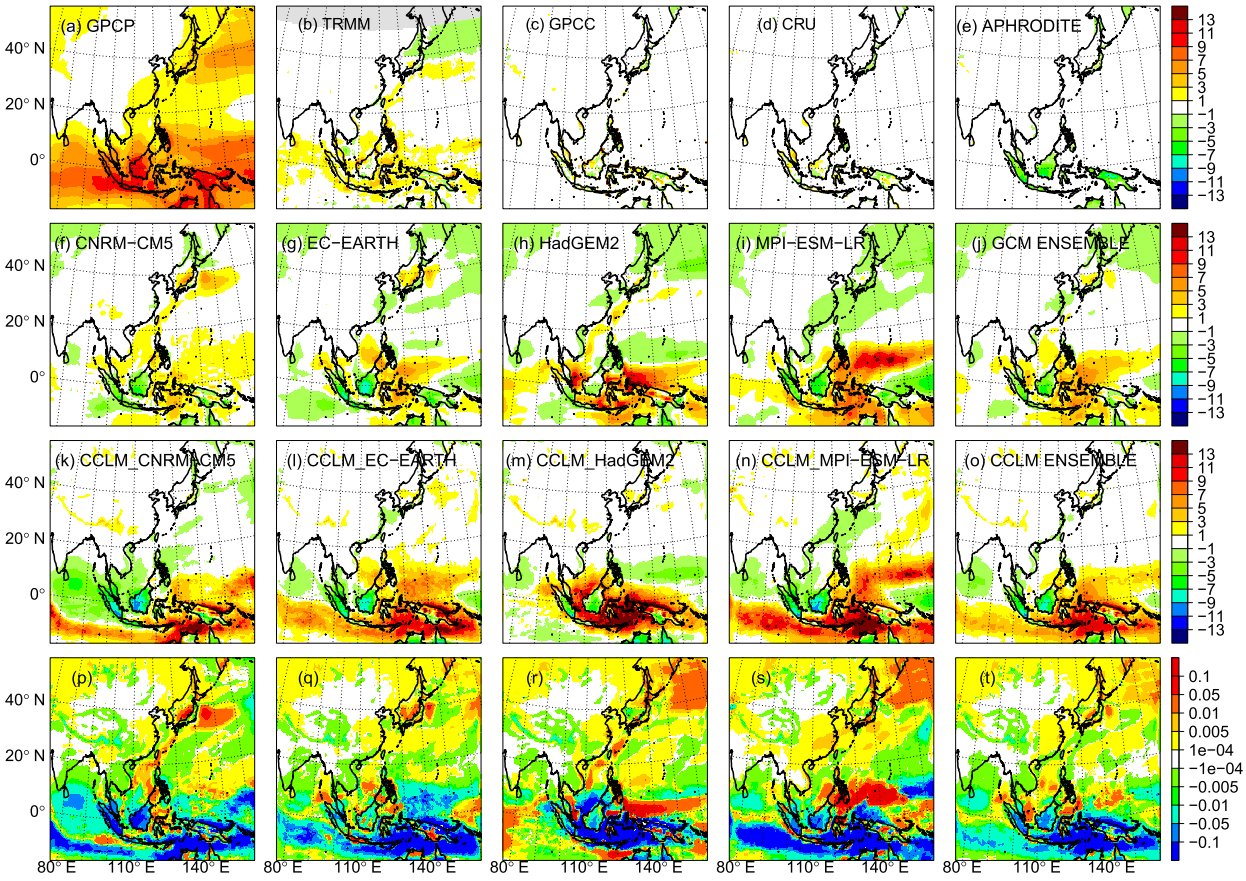

FIG. 5. (a) Observed seasonal mean rainfall (mm day^{-1}) derived from GPCP for the DJF for December 1996–November 2005. Biases of (b) TRMM (December 1998–November 2005), (c) GPCC, (d) CRU, and (e) APHRODITE (December 1996–November 2005) against GPCP. (f)–(o) Biases of the GCMs and CCLM simulations and corresponding ensemble means against GPCP. (p)–(t) Added value index of seasonal mean rainfall for each GCM–CCLM combination. Note that the GPCC, CRU, and APHRODITE datasets only cover land areas.

which is not the case for the winter. Figures 4e and 4f show that the error variance for 2-m temperatures of GCM and CCLM simulations is smaller for the summer than for the winter for the MG, NE, KJ, and land regions. STDE values are mostly less than 2.5°C for the summer for most subregions except for those of the WC, whereas in winter model results show error variances exceeding values of 3°C for regions such as the WC and MG. In addition, consistent error variance reduction is achieved by downscaling the KJ region for both seasons. STDE values of the reanalysis datasets are less than those of the GCMs and CCLM simulations for most cases, but they still present uncertainties among regions, seasons, and datasets of 0.5°–2.5°C.

b. Precipitation climatology

Figures 5 and 6 show spatial distributions of mean biases of modeled precipitation for the winter and summer and the added value index for the period December 1996–November 2005. From the GPCP climatological mean, we present two prominent rainfall bands for the winter: one located over the tropical region around the equator (rainband 1) and another positioned over the northwestern Pacific Ocean region, east of Japan (rainband 2). Precipitation intensities measured for the central areas of these two rainbands exceed values of 6 mm day^{-1}. TRMM data generally show higher rainfall levels for rainband 1 by 1–3 mm day^{-1} and show less rainfall for rainband 2 by 1–3 mm day^{-1}. Across the land areas (Figs. 5b–e), observation uncertainties are mainly found for the Maritime Continent and for Japan by generally less than 3 mm day^{-1}; however, APHRODITE can underestimate GPCP values for the Maritime Continent by more than 5 mm day^{-1}.

According to the modeled results, rainband 1 precipitation occurring over water bodies is generally overestimated by the GCMs and by CCLM simulations and especially by HadGEM2 and MPI-ESM-LR (Figs. 5f–o). However, most CCLM overestimations for rainband 1 are greater than those of the driving GCMs with values

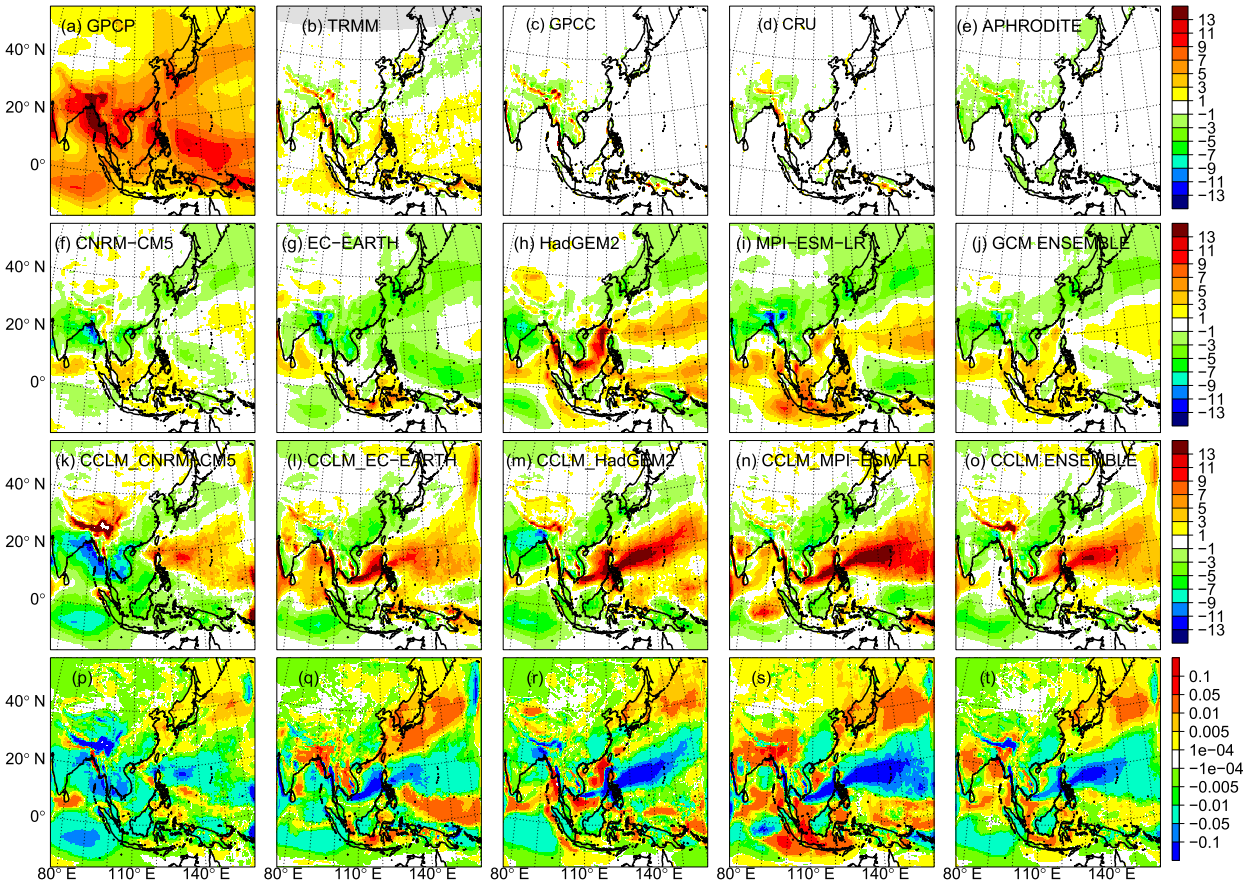

FIG. 6. As in Fig. 5, but for JJA.

reaching in excess of 11 mm day^{-1}. GCM and CCLM results generally underestimate precipitation levels for rainband 1 over land areas with the latter generally making a more significant underestimation than the former. Precipitation occurring over rainband 2 is generally underestimated by the GCMs to values of up to −3 mm day^{-1} with the exception of CNRM-CM5, which overestimates it. Bias observed over rainband 2 is reduced by CCLM as shown in Figs. 5k–o. A comparison of ensemble-mean biases (Figs. 5j,o) shows that both GCM and CCLM ensemble means generally outperform individual model runs.

In terms of added value from downscaling, we see generally consistent spatial patterns of AVI distributions for different GCM–CCLM combinations. Over the equatorial areas, there is generally deterioration (a negative AVI) of climatological means of precipitation for CCLMs. However, across rainband 2, the Sea of Japan, Chinese marginal seas, eastern China, and a large part north of China, AVI values are positive, implying that CCLM can add value to GCMs in terms of precipitation climatology. However, we must note that this added value may be attributed to the referred observations, as we found that, for northern regions reaching 20°N, both the GCM and CCLM can realistically reproduce winter means of observed precipitation from the TRMM bias relative to GPCP (Fig. 5b). The added value derived by downscaling may not be significant relative to observation uncertainties.

For the summer, GPCP observations (Fig. 6a) show strong patterns of precipitation (over 6 mm day^{-1}) widely distributed across the CORDEX-EA domain except for WC and MG and part of the Pacific Ocean. Observed precipitation levels are particularly intense (over 15 mm day^{-1}) along the west flank of the Indo-China Peninsula. We find that uncertainties of the observed precipitation datasets are more pronounced than those for the winter and especially for the Tibetan Plateau, Indo-China Peninsula, and Maritime Continent (Figs. 6b–e). The GCMs show similar patterns of negative biases (Figs. 6f–o) extending from India and the Indo-China Peninsula to SC and KJ. Differences are found as well; we find positive biases in HadGEM2 and MPI-ESM-LR mainly for water bodies positioned

between the equator and 30°N, while this is not the case for the other two GCMs. Some common features of bias distributions are found between the CCLM simulations: a strong positive bias over the northwestern Pacific Ocean between the equator and 30°N and mostly weak negative biases for southern and eastern China, the East China Sea, and the Korean Peninsula. Added value is found for Japan and large water regions surrounding Japan for all GCM–CCLM combinations (Figs. 6p–t). For the other regions, degrees of added value vary from simulation to simulation. MPI-ESM-LR combinations show positive AVI values for the largest fraction of the CORDEX-EA domain.

In comparing Figs. 5 and 6, we find that CNRM-CM5 and EC-EARTH outperform the other two GCMs in reproducing levels of precipitation intensity for the winter and summer and especially for tropical water regions. This feature is partly inherited by corresponding downscaled simulations, which implies that boundary forcing has considerable influence on downscaled results. At the same time, similarities in spatial distribution patterns observed between CCLM simulations are enhanced by downscaling when compared with those of GCMs.

As for the 2-m temperatures, several statistical metrics were used to assess the performance of the examined models in representing precipitation patterns observed across different subregions for the winter and summer (Fig. 7). Biases found for the winter are much less significant than those found for the summer. In the selected subregions and land areas for the winter (Fig. 7a), bias values are generally negative for GCMs, from -0.25 to $-1\,\mathrm{mm\,day^{-1}}$, whereas they are mostly positive for CCLM simulations (0.25–$0.6\,\mathrm{mm\,day^{-1}}$). SC and KJ and the average of land areas show a reduction in winter biases as a result of downscaling based on the ensemble mean. In the summer, biases are generally negative except for those for the WC and MG regions. Negative biases are the largest for the SC and KJ regions. Bias reduction is also found for NE, KJ, and land areas. Furthermore, we find levels of observation uncertainty to be greater for the summer than for the winter and especially for WC, SC, and KJ, for which GCMs and CCLM simulations generally perform unrealistically.

Spatial correlation coefficients between modeled and observed precipitation (Figs. 7c,d) are lower than those for 2-m temperatures (Figs. 4c,d); correlation values are mostly greater than 0.5 but vary from region to region. In the case of the MG region, CORR values are greater for the summer than for the winter and vice versa for the KJ region. Downscaling adds hardly any value to spatial patterns of climatological precipitation found for both the summer and winter. Error variances for the winter are generally smaller than those for the summer. In most cases, values are less than $0.8\,\mathrm{mm\,day^{-1}}$ for the winter for selected subregions while varying strongly from region to region for the summer with smaller error variances found for the MG and NE regions than for the other regions. Furthermore, it can be seen that downscaling hardly contributes to the error variance reduction of modeled precipitation. However, values are comparable to those of other observation datasets in terms of the error variances of most subregions for the winter (Figs. 7e,f).

In summarizing our analysis, we note considerable seasonal variability in spatial distributions of 2-m temperature biases and in added value from CCLM simulations: biases are generally smaller for the summer than for the winter, but areas with added value are larger for the winter. Added value in the winter is mainly found for India and part of northwestern China across all GCM–CCLM combinations. The CNRM-CM5- and HadGEM2-driven runs show larger areas for which added value can be found relative to the other two combinations found for the winter. For precipitation levels, downscaling can add value to GCMs by reducing the bias of part of the domain, but CCLM hardly outperforms GCMs when applied to tropical regions where extreme rainfall patterns are observed. The bias distributions of downscaled runs can be partly inherited from their corresponding GCMs for both variables. At the same time, similarities found between downscaled simulations are more significant than similarities observed between forcing GCMs and especially in the case of summer precipitation (Fig. 6).

c. Precipitation variability and intensity distribution

According the results shown in Fig. 8, we note that observation datasets (GPCP, GPCC, CRU, APHRODITE, and TRMM) are generally consistent in capturing annual cycles of precipitation with the largest values found for the summer and with the lowest values found for the winter across all regions. In particular, the SC and KJ regions show the most intense rainfall peaks in the summer relative to those of the other regions. Discrepancies between observations are found. APHRODITE shows less rainfall than the other observations for the summer and particularly when considering the whole land area (Fig. 8g).

The annual precipitation cycle of the KJ region is less satisfactorily simulated by the models especially for the period from July to September, for which both GCM and CCLM simulations show underestimations of more than $2.5\,\mathrm{mm\,day^{-1}}$. Although all of the models exhibit a general capacity to reproduce the general structure of the annual cycle, the models' capacities to represent

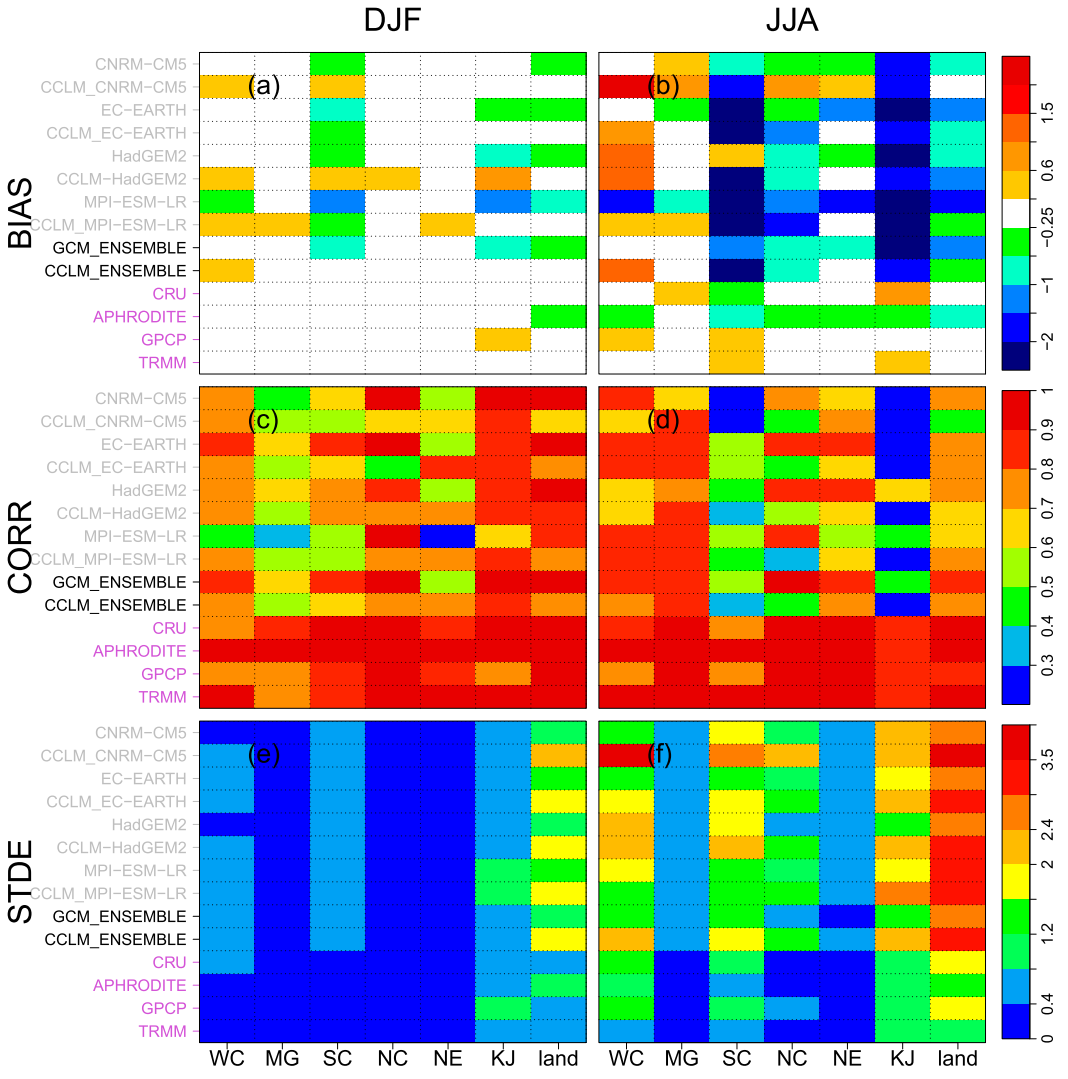

FIG. 7. As in Fig. 4, but for precipitation, with GPCC precipitation used as the reference dataset.

precipitation intensity vary considerably. For GCMs, MPI-ESM-LR generates the worst results, as it underestimates precipitation levels for almost all of the selected regions. CNRM-CM5 and HadGEM2 are generally consistent and are superior to the EC-EARTH in capturing annual cycle variability in precipitation for regions such as MG, SC, and NE and for the whole land area.

For CCLM, downscaled simulations most closely reflect observations (except for APHRODITE) than their GCM counterparts for the whole land area (Fig. 8g) with the exception of that of the HadGEM2 GCM–CCLM combination for May–August. For annual cycle variability of subregions, added value is found to be generated by CCLM_MPI-ESM-LR and MPI-ESM-LR for all regions except for the SC and northern China (NC) regions for the summer. CCLM-CNRM-CM5 performs worse than CNRM-CM5 in WC, MG, NC, and KJ; it outperforms or performs similar to CNRM-CM5 in terms of NE (October–December) and SC (winter half year). CCLM-HadGEM2 adds value to its forcing HadGEM2 over KJ in the winter half year. Deterioration or no obvious improvement by CCLM-HadGEM2 to HadGEM2 is seen in the other subregions. EC-EARTH is closer to observations than CCLM-EC-EARTH in WC. However, their performance varies by region and season without showing consistent patterns in added value for the other subregions.

The box-and-whisker plots in Figs. 9 and 10 show distributions of land-area-averaged daily precipitation for each subregion for the winter and summer, respectively. GPCP observations show that the winter is an arid season for much of the CORDEX-EA region, although considerable variability is found across regions; for instance, KJ is subject to the heaviest rainfall (both the

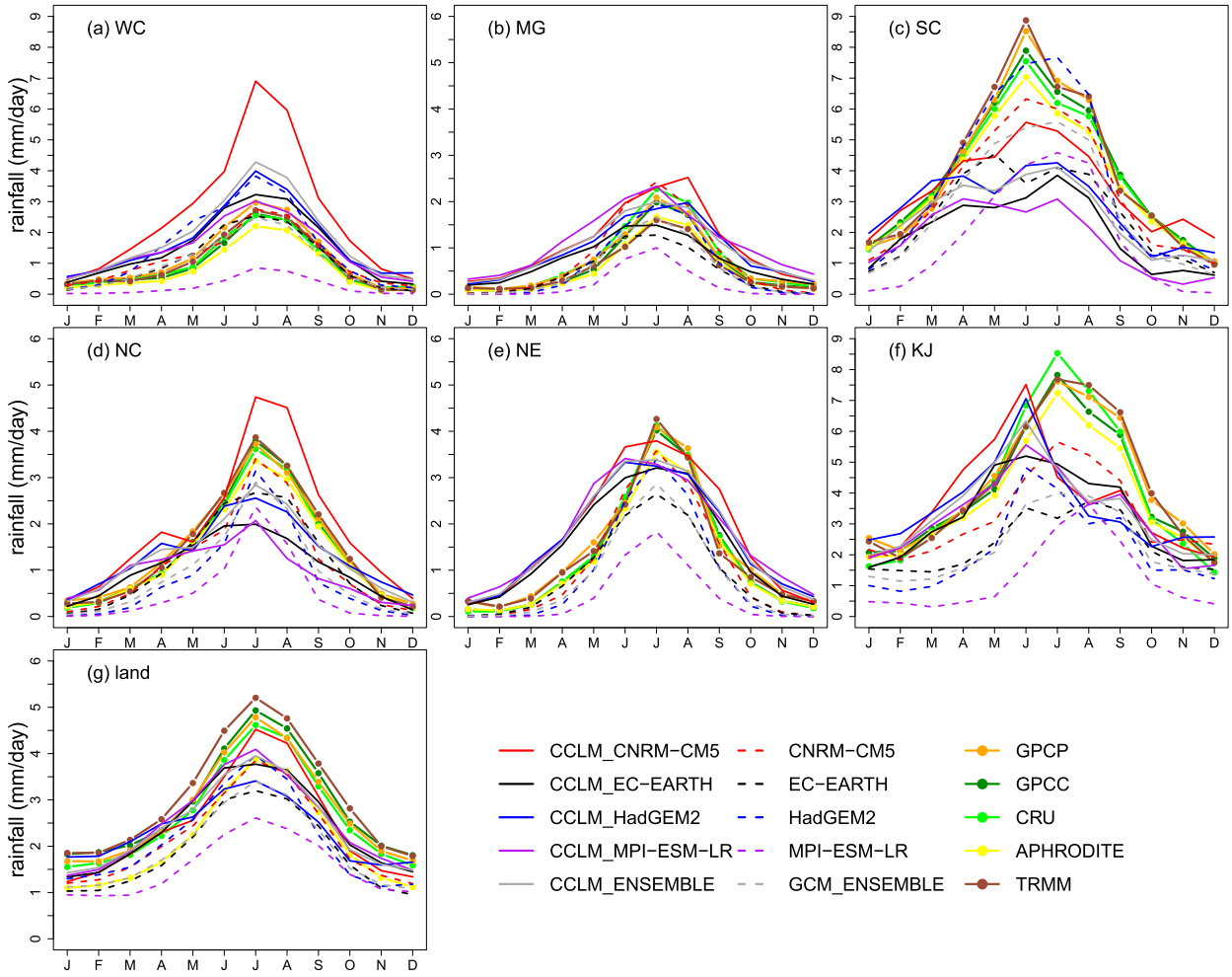

FIG. 8. Mean annual cycle of rainfall (mm day^{-1}) derived from observations (GPCP, GPCC, CRU, APHRODITE, and TRMM), GCMs, and CCLM simulations for six subregions and the land area of the CORDEX-EA domain [the period covers December 1979–November 2005, except for GPCP (December 1996–November 2005) and TRMM (December 1998–November 2005)].

maximum and 95th percentiles of precipitation), with maximum daily rainfall levels exceeding 25 mm day^{-1}; on the other hand, MG is the driest region, with daily precipitation levels of less than 1.5 mm day^{-1}. The range of the precipitation distribution, which is denoted by the distance between the 25th and 75th percentiles, is narrower than or around approximately 0.5 mm day^{-1} for all subregions except for the SC and KJ regions. TRMM rainfall is generally consistent with GPCP in reflecting precipitation distributions for most of the examined regions. Some differences in maximum rainfall levels are observed for SC, NC, and KJ. GCMs hardly reproduce these features of daily precipitation distributions for almost all of the subregions.

Extreme rainfall patterns are largely underestimated by GCMs with the range of simulated daily precipitation typically being much narrower than observed ranges, especially for MG, NC, and NE. Of the GCMs examined, MPI-ESM-LR is the worst in representing observed precipitation distributions. In comparison, CCLM simulations add value to GCMs in representing precipitation distributions. The intensities of extreme precipitation simulated by CCLMs generally reflect GPCP observations better than that of GCMs. The spatial variability of observed extreme rainfall levels is also better reproduced by CCLM than by GCMs. The precipitation range of CCLM simulations is in better agreement with observations than those of GCMs. No CCLM simulation can outperform the other simulations for all subregions, but we note that CCLM_HadGEM2 is the best of the GCM and CCLM runs in capturing GPCP winter rainfall distributions for land regions (Fig. 9g), and the improvement by CCLM for MPI-ESM-LR combination is more apparent than those for other combinations.

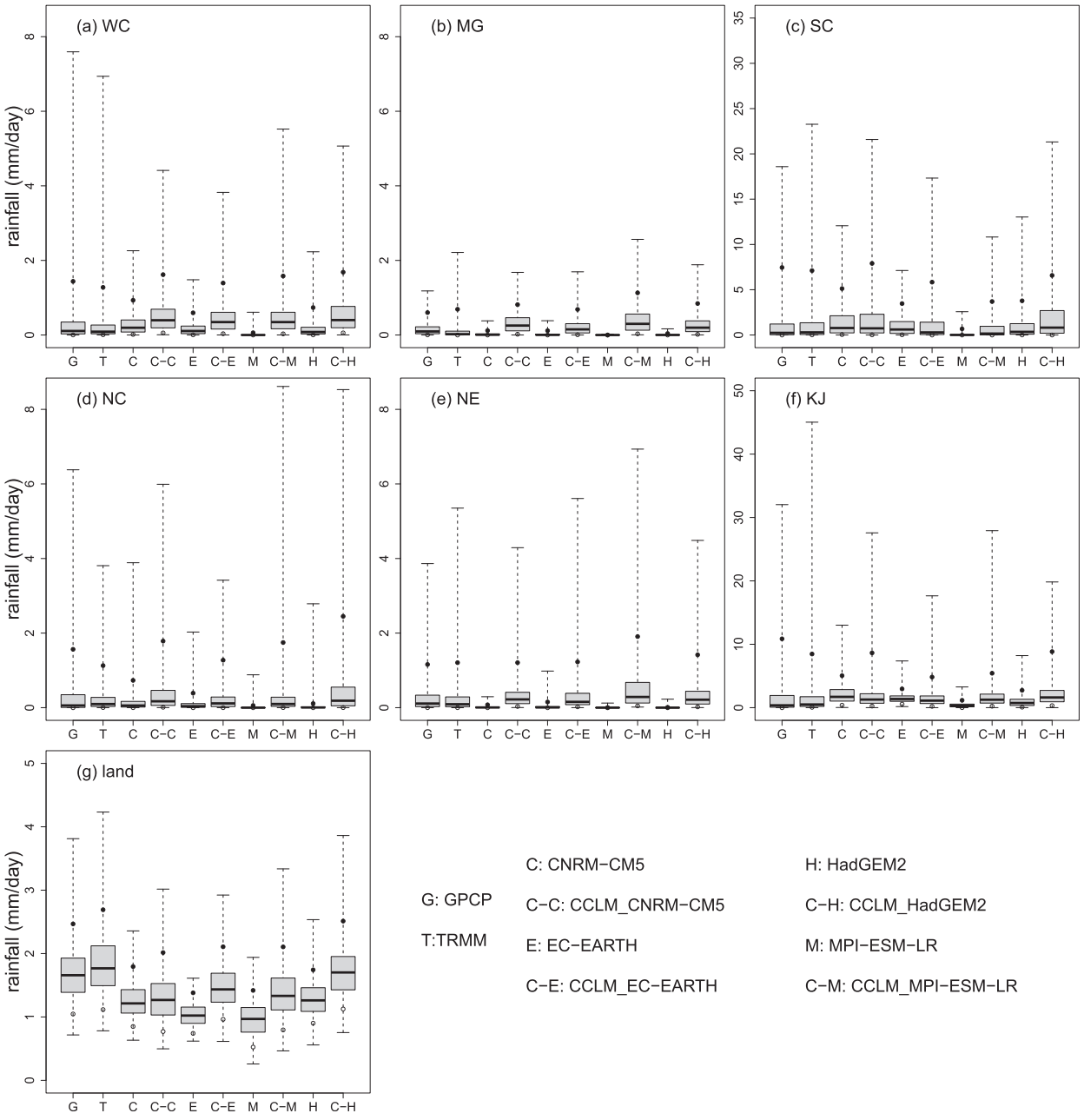

FIG. 9. Box-and-whisker plots for the six subregions and the land area of the domain for the rainfall distribution of the DJF. The base and top of the box denote the 25th and 75th percentiles, respectively; the band within the box is the median; ends of the whiskers represent minimum and maximum values; and the black circle and black point denote the 5th and 95th percentiles, respectively. Note that there are differences in the various *y* axes. [The period covers DJF of December 1996–November 2005, except for TRMM (DJF of June 1998–November 2005)].

In contrast, the summer is the rainy season for the CORDEX-EA region. Precipitation intensity levels vary strongly from region to region (Fig. 10). Features of GPCP and TRMM are generally similar across most subregions. For the selected subregions, SC and KJ are characterized by the highest maximum precipitation levels (>30 mm day^{-1}). MG is the most arid region in the summer as it is in the winter, with area-mean maximum precipitation levels reaching 8 mm day^{-1}. The precipitation range is much broader in the summer than in the winter. The land-area-averaged daily precipitation (Fig. 10g) generally ranges from 3 to

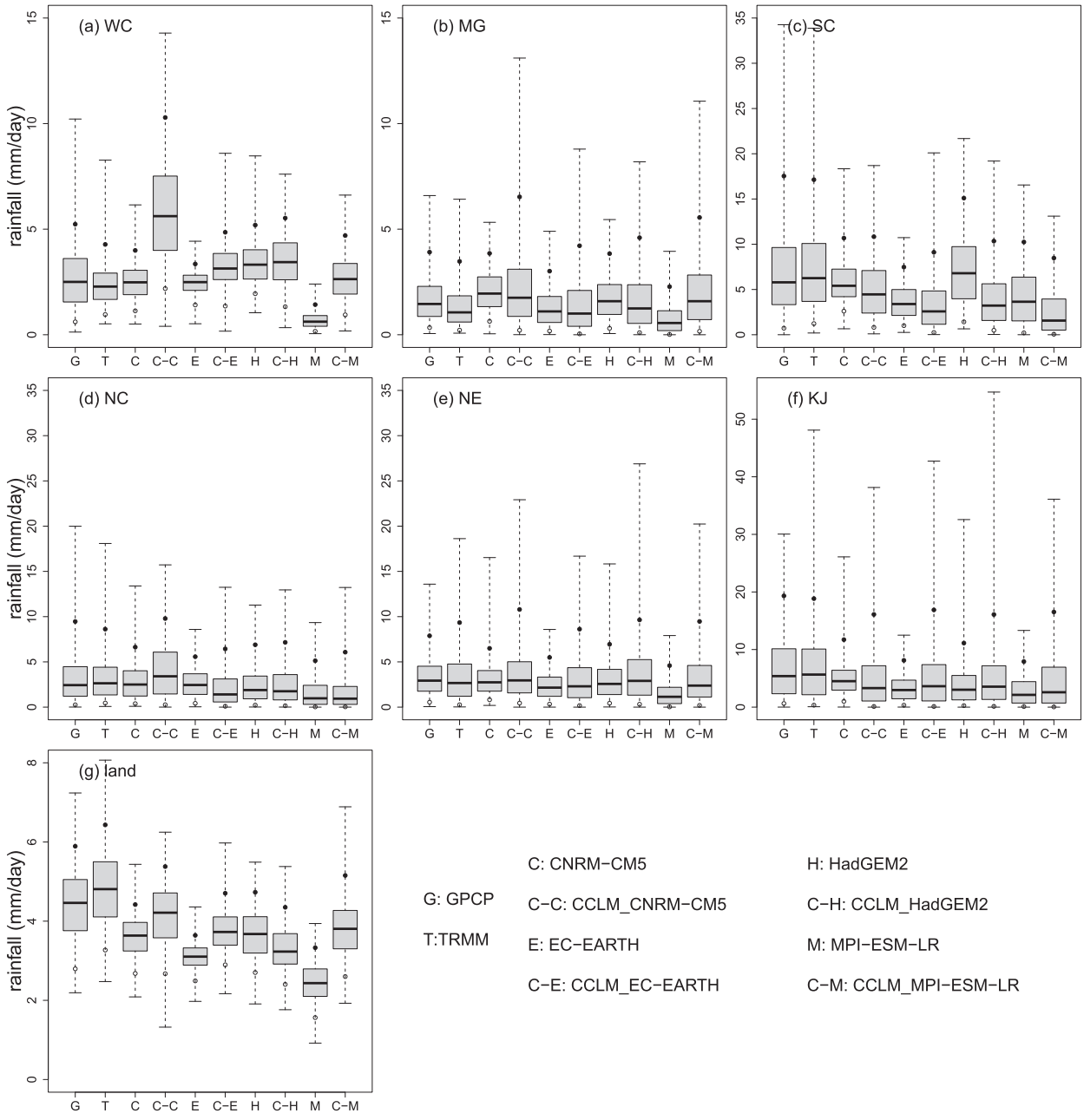

FIG. 10. As in Fig. 9, but for JJA.

6 mm day^{-1}. The precipitation distribution of GCMs is in better agreement with observed precipitation in the summer than that in the winter for the MG, NC, and NE regions. As was found in the winter season, MPI-ESM-LR is generally the least effective at simulating precipitation distributions among the GCMs. CCLM_MPI-ESM-LR also ranks as the least effective of the CCLM simulations, but it adds value to MPI-ESM-LR for most regions. CCLM simulations are in better agreement with observations than GCMs in reproducing extreme or precipitation ranges for the NC, NE, KJ, and land regions, which is not found to be the case for the other subregions.

d. Large-scale circulation in the lower troposphere

The amount of water vapor is generally linked to the atmosphere's potential capacity for precipitation (Zhou and Yu 2005). To investigate mechanisms that may control precipitation climatological mean bias and seasonal variability, we compared seasonal means of the

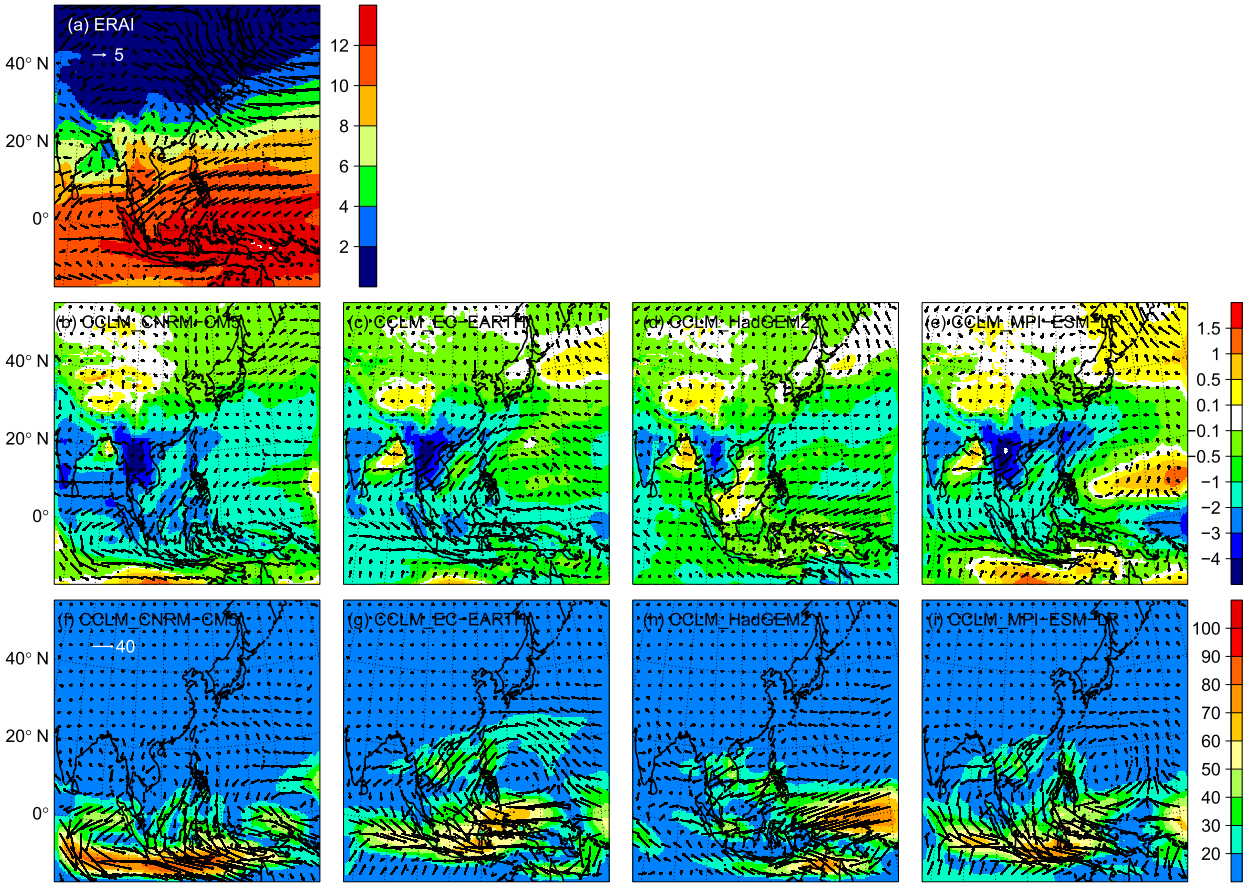

FIG. 11. (a) Winter (DJF) mean water vapor mixing ratio (shading; $g\,kg^{-1}$) and wind vectors (arrows; $m\,s^{-1}$) for the ERAI reanalysis, and (b)–(e) biases of four CCLM simulations relative to (a). (f)–(i) Biases in the water vapor transport (shading and arrows; $m\,s^{-1}\,g\,kg^{-1}$) of CCLM simulations against ERAI reanalysis data for December 1996–November 2005 at the 850-hPa pressure level.

modeled water vapor mixing ratio, wind vectors, and water vapor transport in the lower troposphere at 850 hPa with those derived from ERAI for the winter (Fig. 11) and summer (Fig. 12).

Figure 11a shows that water vapor mixing ratios generally decrease from the equator to high latitudes in the winter, exceeding values of $10\,g\,kg^{-1}$ for the tropical region and measured at less than $2\,g\,kg^{-1}$ for most regions north of 30°N. The spatial distribution of the winter mean water vapor mixing ratio is similar to that of GPCP mean precipitation (Fig. 5a). For the summer (Fig. 12a) we find that the water vapor mixing ratio generally intensifies (to over $12\,g\,kg^{-1}$ in regions lying between 10° and 30°N) and shifts northward relative to that of the winter. At the same time, the rainfall band moves northward (Fig. 6a) and covers similar regions as those of the water vapor mixing ratio. This result indicates that water vapor levels set the basis of seasonal variability in precipitation climatological means, which is further verified by the large spatial correlation coefficient found (of generally larger than 0.6) between seasonal mean precipitation and water vapor amount for observations or model data (now shown here).

Reanalyzed winter features of the water vapor mixing ratio and large–scale circulations are generally satisfactorily simulated by all four CCLM simulations for land regions north of 30°N, while this is not the case for tropical regions, for which significant biases in water vapor and wind speed values are generally found (Figs. 11b–e). Large wind biases are also found for regions northeast of Japan. The overestimated air pressure found for the Tibetan Plateau and for the northwestern Pacific Ocean east of Japan and underestimated air pressure found for tropical regions are supposed to result in the biased winds especially over water regions (see Fig. S3 in the online supplemental material).

In addition, it can be observed that winter precipitation biases of the CCLM simulations (Figs. 5k–o) are closely related to biases of water vapor transport (Figs. 11f–i); overestimated precipitation for some tropical

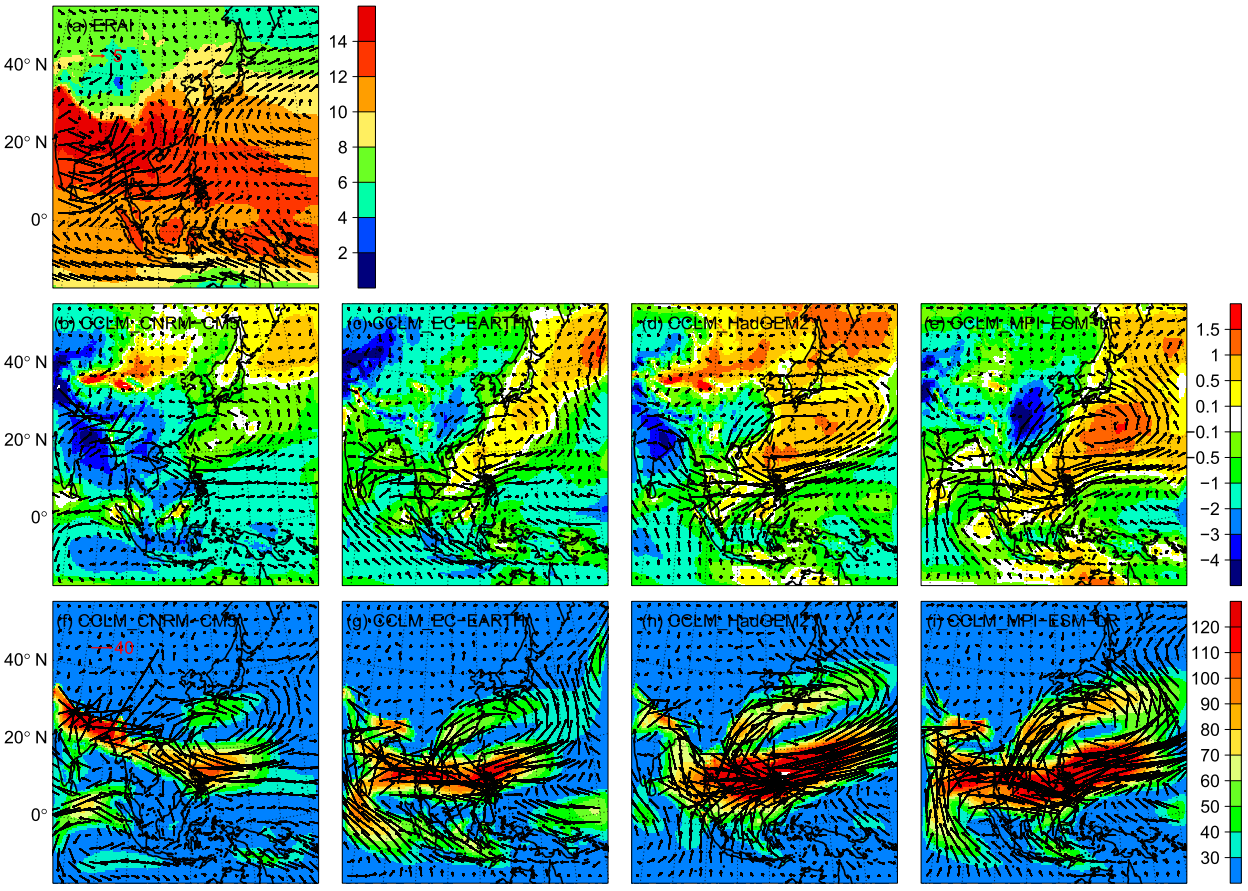

FIG. 12. As in Fig. 11, but for JJA.

regions is mainly a result of an overestimated convergence of water vapor transport found for tropical regions in all CCLM simulations. CCLM_HadGEM2 outperforms the other CCLM simulations for some tropical regions in terms of water vapor mixing ratios, wind fields, and water vapor transport, thus performing the best of the CCLM simulations in generating winter precipitation patterns (Fig. 5) for these regions.

In the summer, precipitation in East Asia is derived from three main sources (Fig. 12a): 1) strong southwesterly winds from the Indian summer monsoon, 2) southerly and southeasterly winds from the west Pacific, and 3) cross-equatorial winds. Simulated biases of low-level circulation will influence associated amount of water vapor transport.

We find pronounced eastward and northeastward shifts in western Pacific subtropical highs from our simulations (Figs. S4b–e in the online supplemental material). In addition, the pressure bias patterns are generally consistent across all simulations (see Figs. S4g–j). A pattern of positive (weak negative), strongly negative, and positive (weak negative) is observed from north to south with a strong negative pressure bias found for regions spanning the Tibetan Plateau–South China to the northwestern Pacific Ocean from 15° to 30°N, generating apparent cyclonic wind biases (Figs. S4g–j). Biases in simulating large-scale circulation and related water vapor transport result in rainfall underestimations for South China and overestimations for regions ranging from the South China Sea to the northwestern Pacific Ocean (Figs. 6k–o). Specifically, northeasterly biases over South China derived from CCLM simulations (Figs. 12b–e) lead to lower levels of water vapor transport and a negative precipitation bias found over South China (Figs. 6k–o). A cyclonic wind bias (Figs. 12b–e) is supposed to cause overestimation of the convergence of water vapor transport (Figs. 12f–i) and associated overestimated summer precipitation for regions spanning the South China Sea to the northwestern Pacific Ocean (Figs. 6k–o).

As a short summary, we find strong spatial variability in CCLM simulations reproducing low-level circulations and related water vapor transport processes. Less optimal results are found for tropical regions for the winter and for the South China Sea and northwestern Pacific

Ocean for the summer, meaning that CCLM simulations poorly reproduce precipitation climatological means for these regions. Limited capacities to model western Pacific subtropical highs and associated cyclonic wind biases for the summer are also found for some GCMs of the CMIP3 and CMIP5 (Feng et al. 2014; Song and Zhou 2014) and for RCM models (Niu et al. 2015). This scenario may be a result of an unrealistic configuration of the Tibetan Plateau, with simulated large biases in pressure systems derived for both the winter and summer (Figs. S3 and S4 in the online supplemental material), which may heavily influence the climate modeling of (thermo-) dynamic processes for the CORDEX-EA region (Wang et al. 2008). Model physics and parameterizations, especially in terms of convection scheme selection may also greatly affect low-level circulation and precipitation modeling capacities (Niu et al. 2015).

4. Climate extremes—Precipitation relevant

Extreme climate events have serious impacts on land and marine environments and on human activities. These events involve high levels of spatial and temporal variability, especially at regional or local scales. It is challenging yet important for climate models to reproduce features of climate extremes. Here, the capacity of GCMs and CCLM simulations to reproduce relevant precipitation extremes is assessed by comparing them against GPCP observations for 1996–2005. Three precipitation-relevant extreme climate indices drawn from a set of 27 extreme indices defined by the Expert Team on Climate Change Detection and Indices (ETCCDI; Frich et al. 2002; Zhang et al. 2011) are used: the simple daily intensity index (SDII; annual mean precipitation measured for wet days at precipitation $\geq 1.0\,\text{mm day}^{-1}$), the consecutive dry day (CDD; annual maximum number of consecutive days with precipitation $< 1.0\,\text{mm day}^{-1}$), and the consecutive wet day (CWD; annual maximum number of consecutive days with precipitation $\geq 1.0\,\text{mm day}^{-1}$). We expect to find that high-resolution CCLM simulations can add value to GCMs in simulating features of extreme climate events.

Figure 13 shows the spatial distribution of the observed SDII, biases of GCM and CCLM simulations against observations and the added value index. The figure shows that the SDII generally exceeds a value of $4\,\text{mm day}^{-1}$ over the CORDEX-EA domain except for inner continental regions such as MG and WC. High SDIIs exceeding $12\,\text{mm day}^{-1}$ are mainly found along coastal areas and in parts of the Pacific and Indian Oceans. The intensity of observed SDII values is generally underestimated by GCMs, especially by CNRM-CM5 and EC-EARTH. HadGEM2 and MPI-ESM-LR generally underestimate observed SDII values for land areas, while they overestimate SDII values for some tropical water regions. CCLM simulations share similar distributions of SDII biases. Overestimations of observed SDII intensities by CCLM simulations are mainly found for NC, MG, the Himalayan region, and most water regions. Extreme overestimations of greater than $9\,\text{mm day}^{-1}$ can be clearly observed in tropical regions, especially in the case of CCLM_HadGEM2 and CCLM_MPI-ESM-LR. Bias reductions achieved by downscaling are mainly found for regions spanning India to Southeast Asia; extending north across eastern China, the Korean Peninsula, and Japan; and covering the Pacific Ocean east of Japan, which is also shown by positive AVI values in Figs. 13l–p.

The observed annual CDD index (Fig. 14a) presents periods of less than 20 days mainly for the tropical region and northwestern Pacific region. A large part of the CORDEX-EA features 20–60 consecutive dry days with the exception of MG, WC, India, and part of the western Pacific region, for which the CDD periods exceed 60 days. There are similarity of CDD biases distributions among four GCMs. The biases are obvious over regions with large observed CDD index. GCMs generally overestimate observed CDD values for most land of the CORDEX-EA region while underestimating CDD values for part of the western Pacific and South China Sea, which is also reflected by GCM ensemble means (Fig. 14f). MPI-ESM-LR is the least effective GCM in reproducing CDD index distributions, which largely overestimate observed CDD for the continental region of the CORDEX-EA. Downscaled results show both improvements and decline relative to driving GCMs. Bias reduction and positive AVI (Figs. 14g–p) derived through downscaling can be detected for land regions north of 30°N. Regions exhibiting decline are mainly distributed across India, the Indo-China Peninsula, parts of the SC, and tropical water regions. The MPI-ESM-LR-driven simulation (Fig. 14o) features the largest regions with positive AVI values relative to those of the other three simulations.

Figure 15a shows that the observed annual CWD for tropical land regions and for the west coast of the Indo-China Peninsula can exceed 40 days but are less than 15 days for regions north of 30°N. Northwestern China presents the lowest CWD values (<5 days). CWD indices are generally overestimated by more than 20 days for the region south of 30°N for CNRM-CM5, EC-EARTH, and HadGEM2. Biases of the CWD index of MPI-ESM-LR are much smaller than those of the other three GCMs. Added value is achieved by downscaling in reproducing the CWD index (Figs. 15g–p). Biases of the CWD index of downscaled results mostly fall within ±20 days except for those for some tropical regions and for part of the Tibetan Plateau. Spatial distributions of the

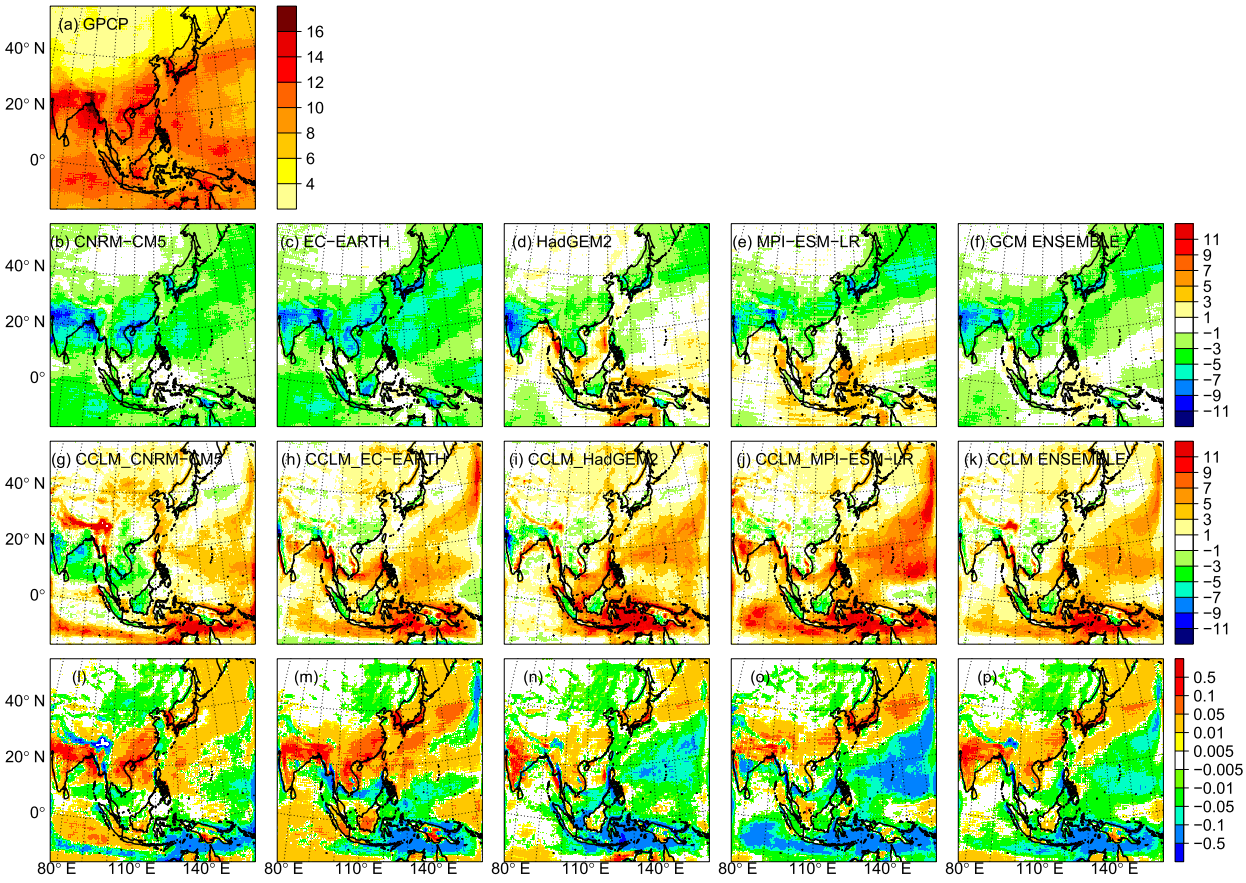

FIG. 13. (a) Mean precipitation amount (mm) for wet days with precipitation levels of ≥1.0 mm (SDII) for GPCP for December 1996–November 2005. Biases (mm) of (b)–(f) GCMs and (g)–(k) CCLM simulations and their ensemble means relative to GPCP. (l)–(p) Added value index for the SDII for each GCM–CCLM combination.

CWD index are very similar for CCLM_EC-EARTH, CCLM_HadGEM2, and CCLM_MPI-ESM-LR. Across all GCM–CCLM combinations, the CNRM-CM5 GCM–CCLM combination (Figs. 15g,l) offers the most added value by downscaling, while the MPI-ESM-LR GCM–CCLM combination (Figs. 15j,o) offers the least amount of added value. The added value for the tropical region south of 20°N is more apparent, presenting large observed CWD values (Fig. 15a), which are greatly overestimated by GCMs (Figs. 15b–f).

5. Summary and concluding remarks

In this study, several CCLM simulations were conducted over the CORDEX-EA domain following CORDEX initiatives using four CMIP5 GCMs (CNRM-CM5, EC-EARTH, HadGEM2, and MPI-ESM-LR) as forcing fields. The modeled outputs were assessed against five observation datasets (i.e., GPCP, GPCC, CRU, TRMM, and APHRODITE) and three of the most current reanalysis datasets (ERAI, JRA-55, and MERRA-2). We address mainly three questions. First, can CCLM simulations realistically reproduce general features of historical climatic patterns for the CORDEX-EA in terms of temperature and precipitation (e.g., seasonal climatological mean, annual variability and precipitation relevant extremes)? Second, can CCLM simulations add value to forcing GCMs? Third, how large is the uncertainty among observation/reanalysis datasets and corresponding effects on model assessments?

It is found that the performance of downscaled results in reproducing climatological features varies from region to region and is highly dependent on the variable, season, metric, and forcing GCM that are considered. In the winter, negative temperature biases cover most regions except for the MG region, for which a significantly positive temperature bias is found. In the summer, more areas with a positive temperature bias are found. The bias intensities of modeled summer temperatures are generally lower than those of modeled winter temperatures, whereas more areas are afforded added value by downscaling for the winter rather than for the summer.

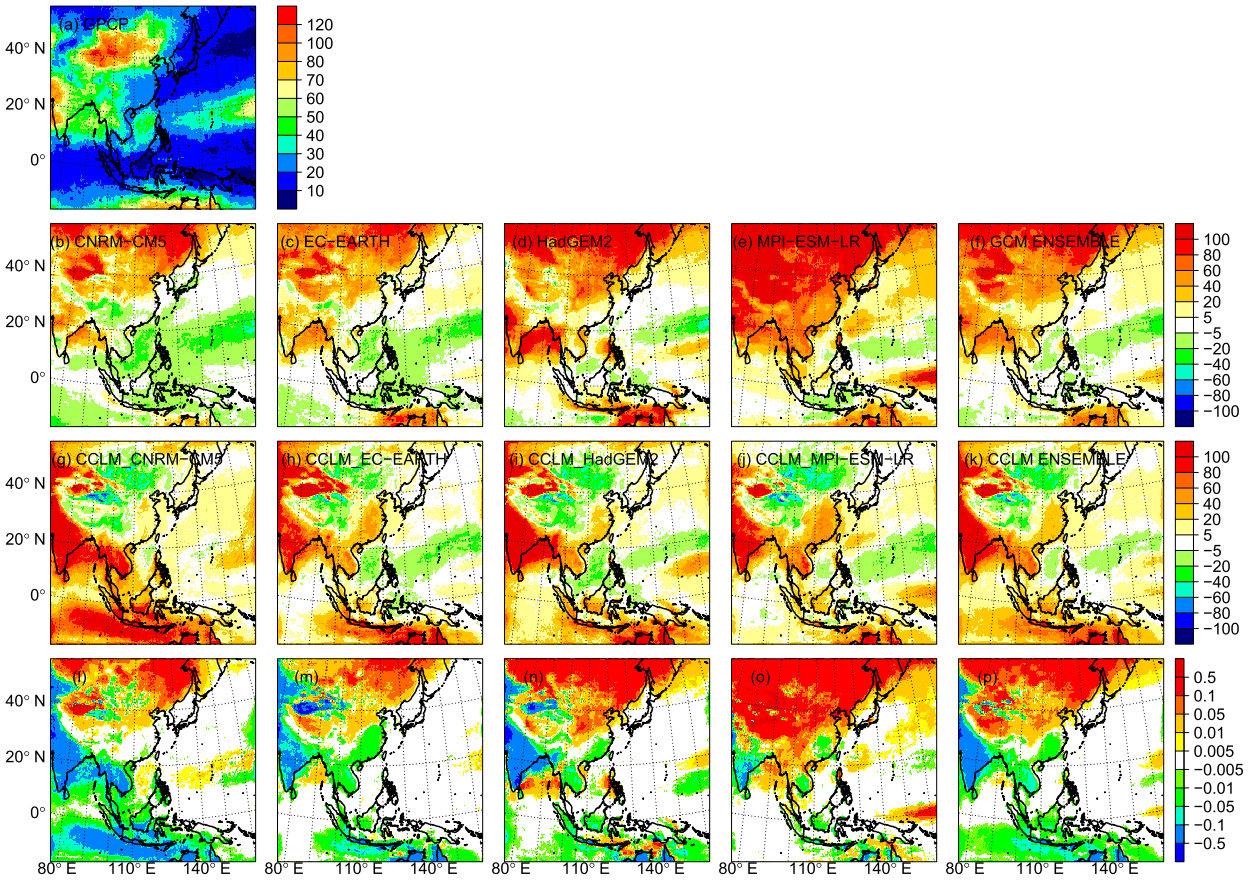

FIG. 14. As in Fig. 13, but for the maximum number of consecutive days with precipitation levels of <1.0 mm (CDD index; days).

For precipitation, downscaling simulations can add value to forcing GCMs for part of the CORDEX-EA region and especially for the winter. However, they do not outperform GCMs in reproducing heavy rainfall patterns for the tropics. CNRM-CM5 and EC-EARTH outperform the other two GCMs in reproducing intensities of precipitation for both the winter and summer, especially for tropical water bodies as found for corresponding downscaling simulations. A consistency of bias distributions found between GCM and CCLM results indicates that biases of GCM forcings are partly inherited by downscaled RCMs, denoting the significance of GCM boundary forcing for downscaling. We find that similarities of spatial patterns of bias distributions among CCLM simulations are much more significant than those of GCM results, revealing a systematic bias resulting from CCLM dynamical processes or parameterization schemes.

The structure of precipitation annual variability can be captured by all GCMs and CCLMs. Four CCLM simulations, not including CCLM_HadGEM2, can add value to GCM forcings in terms of the annual variability of land-area-averaged precipitation. However, no consistent pattern of added value is found for subregions derived from CCLM simulations. CCLM simulations are in better agreement with observations in reproducing area-averaged daily precipitation distributions for the winter than GCMs, especially in the case of MPI-ESM-LR GCM–CCLM combinations. However, no obvious improvement results from downscaling to GCMs for the summer for area-averaged daily precipitation distributions.

Concerning precipitation extremes, CCLM simulations show obvious added value to GCMs in generating observed consecutive wet days (CWD index) for tropical regions. We also find obvious added value from reproducing consecutive dry days (CDD index) over land regions north of 30°N. Pronounced signs of improvement and deterioration are observed when downscaling to GCMs in the case of the simple daily intensity index. Furthermore, we found high levels of seasonal dependence for extreme precipitation indices; spatial patterns of the annual SDII and CWD index mainly resemble those of the summer, whereas spatial patterns of annual CDD index are greatly dependent on winter CDD indices (not shown here). Further evaluations should perform more detailed studies of seasonal rainfall extremes.

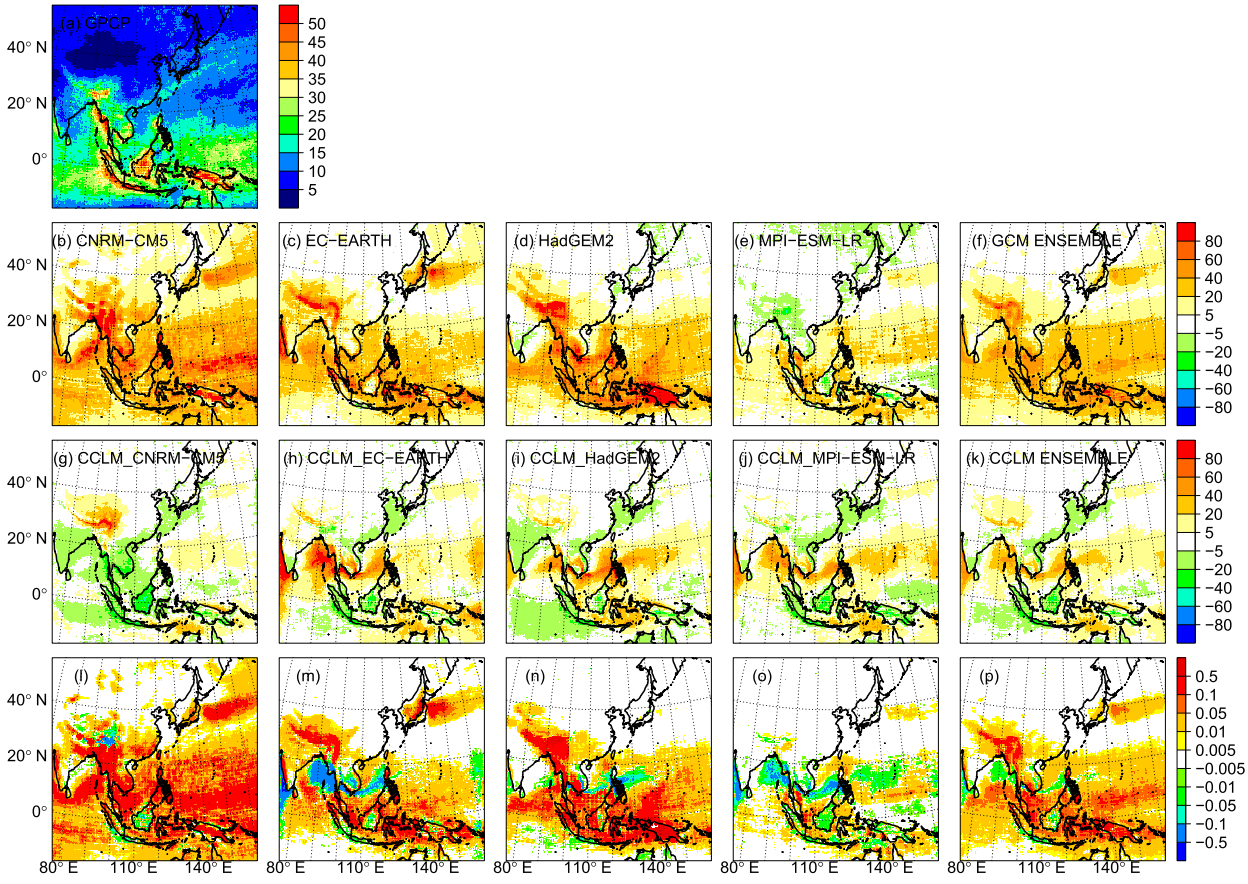

FIG. 15. As in Fig. 13, but for the maximum number of consecutive days with precipitation levels of ≥1.0 mm (CWD index; days).

We note a considerable discrepancy among reanalysis datasets or observation datasets in reflecting precipitation or temperature features for certain regions. Such uncertainties can be as significant as typical biases of GCMs and CCLM simulations (based on a specific observation dataset). For instance, we find a positive temperature bias for Mongolia and for part of northeastern China for the winter from three reanalysis datasets (Figs. 2b–d) and high levels of variability among observation datasets of temperature climatological means for western China (Figs. S1 and S2 in the online supplemental material), and in summer precipitation means for part of the Tibetan Plateau and Maritime Continent (Figs. 6b–e). This implies that, although CCLM simulations may not be able to add value to GCMs, simulated results for some (deterioration) regions can be acceptable relative to those of reanalysis datasets or observation uncertainties. On the other hand, the use of a different reference dataset may result in nonadded value by downscaling for some regions as is shown in Fig. 8 for annual variability in rainfall for land areas using APHRODITE as a reference. Therefore, a careful selection of reference datasets is recommended not only when evaluating modeled climate extremes (Sillmann et al. 2013) but also in terms of climate mean evaluations.

Furthermore, note that only one regional climate model, CCLM, was used in this study. Uncertainties related to using different RCMs to generate climate features for East Asia were not investigated. From previous studies (Gao et al. 2012b; Niu et al. 2015; Gao and Chen 2017; Zhou et al. 2016), we found that most RCMs are able to capture general features of seasonal means and annual cycles of surface temperature and precipitation. However, model performance varies across subregions and seasons, with similarities and differences found among models. Cold and wet biases are derived from most RCMs in generating summer climates of the Tibetan Plateau because of the limited applicability of modern land surface models to the Tibetan Plateau region (Yang et al. 2005; Gao and Chen 2017). Land surface schemes regulate the vertical profiles of atmospheric temperature and horizontal patterns of moisture advection, greatly determining the climatological means and spatial patterns of temperature and precipitation.

As shown from results of some RCMs (Huang et al. 2015), observed precipitation is overestimated for the northwestern Pacific Ocean for the summer and for equatorial regions in the winter. However, these results differ from those of CCLM simulations conducted by Zhou et al. (2016). We found that these significant positive biases are partially inherited from forcing reanalyses/GCMs, although the dynamic setups (regions, physical parameterizations, and resolutions) of individual models are mainly meant to contribute to generated biases.

To improve the capacity for the RCM to simulate regional climate features, it is important to further advance the development of model physics and parameterization schemes of both forcing GCM and RCM. On one hand, the misrepresentation of large-scale features by forcing GCMs can be limited; on the other hand, advanced soil, convection, and other parameterization schemes used in RCM have potential to reduce systematic biases of climatic features, which is particularly true for the tropics, where small-scale convection patterns are an important process. The development and optimization of a convection scheme are supposed to have more significance for improvement of tropical climate modeling than simply increasing model resolutions. Specific attention should also be paid to the modeling of specific regions or circulation systems such as the Tibetan Plateau and western Pacific subtropical high, which have significant effects on the climate systems of East Asia and play an important role in enhancing overall model performance. Efforts to optimize model setups (e.g., domain size selection, sponge zones, or the adoption of spectral nudging) would also contribute to the improvement of model results. Furthermore, we found that ensemble means of GCMs and CCLM simulations outperform individual simulations in reproducing climate features such as climatological means of winter precipitation. To limit random errors and to assess model uncertainties in simulating climate features, large-member ensemble simulations that consider different forcing GCMs, multiple RCMs, and multiple patterns of perturbed physics must be conducted.

In this study, we mainly assessed the capacities and added value of RCM in reproducing climatological means, variability, and extreme indices of precipitation. The capacity for the RCM to simulate short-term variability (e.g., diurnal cycles and intraseasonal variability) has not been investigated and would require the use of high-resolution datasets. Model capacity to simulate temperature extremes and other extreme rainfall events is also not considered. These issues require further investigation.

Acknowledgments. Thanks are given to the three reviewers (Masato I. Nodzu and two anonymous reviewers) for their constructive comments and helpful suggestions. CCLM is a community model from German climate research (www.clm-community.eu). We acknowledge the German Climate Computing Center (DKRZ) for providing computer hardware for our simulations conducted under a project titled "Regional Atmospheric Modeling." Publicly accessible datasets used in the study are greatly appreciated. We thank Burkhardt Rockel for his assistance with regional climate modeling. We also thank Zhengyu Han for his help in observation data collecting. Funding for this study was provided through the National Key Research and Development Program of China (2017YFA0604101), from the National Natural Science Foundation of China (41706019), from the Youth Innovation Promotion Association of the Chinese Academy of Sciences (CAS), from the CAS Interdisciplinary Innovation Team, through the Key Research Program of Frontier Sciences of the CAS, from the General Financial Grant (2017M612357), and from the Special Financial Grant (2017T100520) under the China Postdoctoral Science Foundation.

REFERENCES

Bao, J. W., J. M. Feng, and Y. L. Wang, 2015: Dynamical downscaling simulation and future projection of precipitation over China. *J. Geophys. Res. Atmos.*, **120**, 8227–8243, https://doi.org/10.1002/2015JD023275.

Brown, J. R., C. Jakob, and J. M. Haynes, 2010: An evaluation of rainfall frequency and intensity over the Australian region in a global climate model. *J. Climate*, **23**, 6504–6525, https://doi.org/10.1175/2010JCLI3571.1.

Chen, L., and O. W. Frauenfeld, 2014: A comprehensive evaluation of precipitation simulations over China based on CMIP5 multimodel ensemble projections: CMIP5 precipitation in China. *J. Geophys. Res. Atmos.*, **119**, 5767–5786, https://doi.org/10.1002/2013JD021190.

Christensen, J. H., T. R. Carter, M. Rummukainen, and G. Amanatidis, 2007: Evaluating the performance and utility of regional climate models: The PRUDENCE project. *Climatic Change*, **81** (Suppl. 1), 1–6, https://doi.org/10.1007/s10584-006-9211-6.

Collins, and Coauthors, 2011: Development and evaluation of an Earth-system model—HadGEM2. *Geosci. Model Dev.*, **4**, 1051–1075, https://doi.org/10.5194/gmd-4-1051-2011.

Dee, D. P., and Coauthors, 2011: The ERA-Interim reanalysis: Configuration and performance of the data assimilation system. *Quart. J. Roy. Meteor. Soc.*, **137**, 553–597, https://doi.org/10.1002/qj.828.

Dosio, A., H. J. Panitz, M. Schubert-Frisius, and D. Luthi, 2015: Dynamical downscaling of CMIP5 global circulation models over CORDEX-Africa with COSMO-CLM: Evaluation over the present climate and analysis of the added value. *Climate Dyn.*, **44**, 2637–2661, https://doi.org/10.1007/s00382-014-2262-x.

Fekete, B. M., C. J. Vörösmarty, J. O. Roads, and C. J. Willmott, 2004: Uncertainties in precipitation and their impacts on runoff estimates. *J. Climate*, **17**, 294–304, https://doi.org/10.1175/1520-0442(2004)017<0294:UIPATI>2.0.CO;2.

Feng, J., T. Wei, W. Dong, Q. Wu, and Y. Wang, 2014: CMIP5/AMIP GCM simulations of East Asian summer monsoon.

Adv. Atmos. Sci., **31**, 836–850, https://doi.org/10.1007/s00376-013-3131-y.

Feser, F., B. Rockel, H. von Storch, J. Winterfeldt, and M. Zahn, 2011: Regional climate models add value to global model data: A review and selected examples. *Bull. Amer. Meteor. Soc.*, **92**, 1181–1192, https://doi.org/10.1175/2011BAMS3061.1.

Frich, P., L. V. Alexander, P. M. Della-Marta, B. Gleason, M. Haylock, A. Klein Tank, and T. Peterson, 2002: Observed coherent changes in climatic extremes during the second half of the twentieth century. *Climate Res.*, **19**, 193–212, https://doi.org/10.3354/cr019193.

Fu, C., and Coauthors, 2005: Regional Climate Model Intercomparison Project for Asia. *Bull. Amer. Meteor. Soc.*, **86**, 257–266, https://doi.org/10.1175/BAMS-86-2-257.

Gao, X., Z. Zhao, and F. Giorgi, 2002: Changes of extreme events in regional climate simulations over East Asia. *Adv. Atmos. Sci.*, **19**, 927–942, https://doi.org/10.1007/s00376-002-0056-2.

——, Y. Shi, D. Zhang, and F. Giorgi, 2012a: Climate change in China in the 21st century as simulated by a high resolution regional climate model. *Chin. Sci. Bull.*, **57**, 1188–1195, https://doi.org/10.1007/s11434-011-4935-8.

——, ——, ——, J. Wu, F. Giorgi, Z. Ji, and Y. Wang, 2012b: Uncertainties in monsoon precipitation projections over China: Results from two high-resolution RCM simulations. *Climate Res.*, **52**, 213–226, https://doi.org/10.3354/cr01084.

Gao, Y., and D. Chen, 2017: Modeling of regional climate over the Tibetan Plateau. *Oxford Research Encyclopedia of Climate Science*, https://doi.org/10.1093/acrefore/9780190228620.013.591.

Gelaro, R., and Coauthors, 2017: The Modern-Era Retrospective Analysis for Research and Applications, version 2 (MERRA-2). *J. Climate*, **30**, 5419–5454, https://doi.org/10.1175/JCLI-D-16-0758.1.

Giorgetta, M., and Coauthors, 2012: CMIP5 simulations of the Max Planck Institute for Meteorology (MPI-M) based on the MPI-ESM-LR model: The historical experiment, served by ESGF. WDC Climate, accessed 6 November 2015, https://doi.org/10.1594/WDCC/CMIP5.MXELhi.

Giorgi, F., and G. T. Bates, 1989: The climatological skill of a regional model over complex terrain. *Mon. Wea. Rev.*, **117**, 2325–2347, https://doi.org/10.1175/1520-0493(1989)117<2325:TCSOAR>2.0.CO;2.

——, C. Jones, and G. R. Asrar, 2009: Addressing climate information needs at the regional level: The CORDEX framework. *WMO Bull.*, **58**, 175–183, http://wcrp.ipsl.jussieu.fr/cordex/documents/CORDEX_giorgi_WMO.pdf.

Guo, Y., W. Dong, F. Ren, Z. Zhao, and J. Huang, 2013: Assessment of CMIP5 simulations for China annual average surface temperature and its comparison with CMIP3 simulations. *Adv. Climate Change Res.*, **9**, 181–186, https://doi.org/10.3969/j.issn.1673-1719.2013.03.004.

Harris, I., P. D. Jones, T. J. Osborn, and D. H. Lister, 2014: Updated high-resolution grids of monthly climatic observations—The CRU TS3.10 dataset. *Int. J. Climatol.*, **34**, 623–642, https://doi.org/10.1002/joc.3711.

Hazeleger, W., and Coauthors, 2010: EC-Earth: A seamless Earth-system prediction approach in action. *Bull. Amer. Meteor. Soc.*, **91**, 1357–1363, https://doi.org/10.1175/2010BAMS2877.1.

Hostetler, S., J. Alder, and A. Allan, 2011: Dynamically downscaled climate simulations over North America: Methods, evaluation, and supporting documentation for users. U.S. Geological Survey Open-File Rep. 2011-1238, 64 pp., https://pubs.usgs.gov/of/2011/1238/pdf/ofr20111238.pdf.

Huang, B., S. Polanski, and U. Cubasch, 2015: Assessment of precipitation climatology in an ensemble of CORDEX-East Asia regional climate simulations. *Climate Res.*, **64**, 141–158, https://doi.org/10.3354/cr01302.

Huang, D.-Q., J. Zhu, Y.-C. Zhang, and A.-N. Huang, 2013: Uncertainties on the simulated summer precipitation over eastern China from the CMIP5 models. *J. Geophys. Res. Atmos.*, **118**, 9035–9047, https://doi.org/10.1002/jgrd.50695.

Huffman, G. J., R. F. Adler, M. M. Morrissey, D. T. Bolvin, S. Curtis, R. Joyce, B. McGavock, and J. Susskind, 2001: Global precipitation at one-degree daily resolution from multisatellite observations. *J. Hydrometeor.*, **2**, 36–50, https://doi.org/10.1175/1525-7541(2001)002<0036:GPAODD>2.0.CO;2.

——, and Coauthors, 2007: The TRMM Multisatellite Precipitation Analysis (TMPA): Quasi-global, multiyear, combined-sensor precipitation estimates at fine scales. *J. Hydrometeor.*, **8**, 38–55, https://doi.org/10.1175/JHM560.1.

IPCC, 2014a: *Climate Change 2014: Impacts, Adaptation, and Vulnerability. Part A: Global and Sectoral Aspects*. C. B. Field et al., Eds., Cambridge University Press, 1132 pp., http://www.ipcc.ch/pdf/assessment-report/ar5/wg2/WGIIAR5-PartA_FINAL.pdf.

——, 2014b: *Climate Change 2014: Impacts, Adaptation, and Vulnerability. Part B: Regional Aspects*. V. R. Barros et al., Eds., Cambridge University Press, 688 pp., http://www.ipcc.ch/pdf/assessment-report/ar5/wg2/WGIIAR5-PartB_FINAL.pdf.

Jacob, D., and Coauthors, 2014: Erratum to: EURO-CORDEX: New high-resolution climate change projections for European impact research. *Reg. Environ. Change*, **14**, 579–581, https://doi.org/10.1007/s10113-014-0587-y.

Ji, Z., and S. Kang, 2015: Evaluation of extreme climate events using a regional climate model for China. *Int. J. Climatol.*, **35**, 888–902, https://doi.org/10.1002/joc.4024.

Kessler, E., 1969: *On the Distribution and Continuity of Water Substance in Atmospheric Circulations*. *Meteor. Monogr.*, No. 32, Amer. Meteor. Soc., 84 pp., https://doi.org/10.1007/978-1-935704-36-2_1.

Kobayashi, S., and Coauthors, 2015: The JRA-55 Reanalysis: General specifications and basic characteristics. *J. Meteor. Soc. Japan Ser. II*, **93**, 5–48, https://doi.org/10.2151/jmsj.2015-001.

Kumar, P., S. Kotlarski, C. Moseley, K. Sieck, H. Frey, M. Stoffel, and D. Jacob, 2015: Response of Karakoram–Himalayan glaciers to climate variability and climatic change: A regional climate model assessment. *Geophys. Res. Lett.*, **42**, 1818–1825, https://doi.org/10.1002/2015GL063392.

Kusunoki, S., R. Mizuta, and M. Matsueda, 2011: Future changes in the East Asian rain band projected by global atmospheric models with 20-km and 60-km grid size. *Climate Dyn.*, **37**, 2481–2493, https://doi.org/10.1007/s00382-011-1000-x.

Lee, J.-W., and S.-Y. Hong, 2014: Potential for added value to downscaled climate extremes over Korea by increased resolution of a regional climate model. *Theor. Appl. Climatol.*, **117**, 667–677, https://doi.org/10.1007/s00704-013-1034-6.

——, ——, E.-C. Chang, M.-S. Suh, and H.-S. Kang, 2014: Assessment of future climate change over East Asia due to the RCP scenarios downscaled by GRIMs-RMP. *Climate Dyn.*, **42**, 733–747, https://doi.org/10.1007/s00382-013-1841-6.

Li, D., 2017: Added value of high-resolution regional climate model: Selected cases over the Bohai Sea and the Yellow Sea areas. *Int. J. Climatol.*, **37**, 169–179, https://doi.org/10.1002/joc.4695.

——, H. von Storch, and B. Geyer, 2016: High-resolution wind hindcast over the Bohai Sea and the Yellow Sea in East Asia: Evaluation and wind climatology analysis. *J. Geophys. Res. Atmos.*, **121**, 111–129, https://doi.org/10.1002/2015JD024177.

Liu, Y., F. Giorgi, and W. M. Washington, 1994: Simulation of summer monsoon climate over East Asia with an NCAR regional climate model. *Mon. Wea. Rev.*, **122**, 2331–2348, https://doi.org/10.1175/1520-0493(1994)122<2331:SOSMCO>2.0.CO;2.

Lott, F., and M. J. Miller, 1997: A new subgrid-scale orographic drag parametrization: Its formulation and testing. *Quart. J. Roy. Meteor. Soc.*, **123**, 101–127, https://doi.org/10.1002/qj.49712353704.

McSweeney, C. F., R. G. Jones, R. W. Lee, and D. P. Rowell, 2015: Selecting CMIP5 GCMs for downscaling over multiple regions. *Climate Dyn.*, **44**, 3237–3260, https://doi.org/10.1007/s00382-014-2418-8.

Mehran, A., A. AghaKouchak, and T. J. Phillips, 2014: Evaluation of CMIP5 continental precipitation simulations relative to satellite-based gauge-adjusted observations. *J. Geophys. Res. Atmos.*, **119**, 1695–1707, https://doi.org/10.1002/2013JD021152.

Niu, X., and Coauthors, 2015: Multimodel ensemble projection of precipitation in eastern China under A1B emission scenario. *J. Geophys. Res. Atmos.*, **120**, 9965–9980, https://doi.org/10.1002/2015JD023853.

Oh, S.-G., J.-H. Park, S.-H. Lee, and M.-S. Suh, 2014: Assessment of the RegCM4 over East Asia and future precipitation change adapted to the RCP scenarios. *J. Geophys. Res. Atmos.*, **119**, 2913–2927, https://doi.org/10.1002/2013JD020693.

Park, C., and Coauthors, 2016: Evaluation of multiple regional climate models for summer climate extremes over East Asia. *Climate Dyn.*, **46**, 2469–2486, https://doi.org/10.1007/s00382-015-2713-z.

Ritter, B., and J.-F. Geleyn, 1992: A comprehensive radiation scheme for numerical weather prediction models with potential applications in climate simulations. *Mon. Wea. Rev.*, **120**, 303–325, https://doi.org/10.1175/1520-0493(1992)120<0303:ACRSFN>2.0.CO;2.

Rockel, B., and B. Geyer, 2008: The performance of the regional climate model CLM in different climate regions, based on the example of precipitation. *Meteor. Z.*, **17**, 487–498, https://doi.org/10.1127/0941-2948/2008/0297.

——, A. Will, and A. Hense, 2008: The Regional Climate Model COSMO-CLM (CCLM). *Meteor. Z.*, **17**, 347–348, https://doi.org/10.1127/0941-2948/2008/0309.

Schättler, U., G. Doms, and C. Schraff, 2018: A description of the nonhydrostatic regional COSMO-Model. Part VII: User's guide (COSMO V5.05). Deutscher Wetterdienst Rep., 175 pp., http://www.cosmo-model.org/content/model/documentation/core/cosmo_userguide_5.05.pdf.

Schneider, U., A. Becker, P. Finger, A. Meyer-Christoffer, M. Ziese, and B. Rudolf, 2014: GPCC's new land surface precipitation climatology based on quality-controlled in situ data and its role in quantifying the global water cycle. *Theor. Appl. Climatol.*, **115**, 15–40, https://doi.org/10.1007/s00704-013-0860-x.

Schrodin, R., and E. Heise, 2002: A new multi-layer soil-model. *COSMO Newsletter*, No. 2, Consortium for Small-Scale Modeling, Offenbach, Germany, 139–151, http://www.cosmo-model.org/content/model/documentation/newsLetters/newsLetter02/newsLetter_02.pdf.

Schulz, J.-P., 2008: Introducing sub-grid scale orographic effects in the COSMO model. *COSMO Newsletter*, No. 9, Consortium for Small-Scale Modeling, Offenbach, Germany, 29–36, http://www.cosmo-model.org/content/model/documentation/newsLetters/newsLetter09/cnl9-06.pdf.

Sillmann, J., V. V. Kharin, X. Zhang, F. W. Zwiers, and D. Bronaugh, 2013: Climate extremes indices in the CMIP5 multimodel ensemble: Part 1. Model evaluation in the present climate. *J. Geophys. Res. Atmos.*, **118**, 1716–1733, https://doi.org/10.1002/jgrd.50203.

Song, F., and T. Zhou, 2014: Interannual variability of East Asian summer monsoon simulated by CMIP3 and CMIP5 AGCMs: Skill dependence on Indian Ocean–western Pacific anticyclone teleconnection. *J. Climate*, **27**, 1679–1697, https://doi.org/10.1175/JCLI-D-13-00248.1.

Sperber, K. R., H. Annamalai, I.-S. Kang, A. Kitoh, A. Moise, A. Turner, B. Wang, and T. Zhou, 2013: The Asian summer monsoon: An intercomparison of CMIP5 vs. CMIP3 simulations of the late 20th century. *Climate Dyn.*, **41**, 2711–2744, https://doi.org/10.1007/s00382-012-1607-6.

Tang, J., and Coauthors, 2016: Building Asian climate change scenario by multi-regional climate models ensemble. Part I: Surface air temperature. *Int. J. Climatol.*, **36**, 4241–4252, https://doi.org/10.1002/joc.4628.

Tiedtke, M., 1989: A comprehensive mass flux scheme for cumulus parameterization in large-scale models. *Mon. Wea. Rev.*, **117**, 1779–1800, https://doi.org/10.1175/1520-0493(1989)117<1779:ACMFSF>2.0.CO;2.

Um, M.-J., Y. Kim, and J. Kim, 2017: Evaluating historical drought characteristics simulated in CORDEX East Asia against observations. *Int. J. Climatol.*, **37**, 4643–4655, https://doi.org/10.1002/joc.5112.

van der Linden, P., and J. F. B. Mitchell, Eds., 2009: ENSEMBLES: Climate change and its impacts—Summary of research and results from the ENSEMBLES project. Met Office Hadley Centre, 160 pp.

Voldoire, A., and Coauthors, 2013: The CNRM-CM5.1 global climate model: Description and basic evaluation. *Climate Dyn.*, **40**, 2091–2121, https://doi.org/10.1007/s00382-011-1259-y.

von Storch, H., and F. W. Zwiers, 1999: *Statistical Analysis in Climate Research.* Cambridge University Press, 484 pp.

——, and Coauthors, 2017: Regional reanalysis without local data: Exploiting the downscaling paradigm. *J. Geophys. Res. Atmos.*, **122**, 8631–8649, https://doi.org/10.1002/2016JD026332.

Wang, B., Q. Bao, B. Hoskins, G. Wu, and Y. Liu, 2008: Tibetan Plateau warming and precipitation changes in East Asia. *Geophys. Res. Lett.*, **35**, L14702, https://doi.org/10.1029/2008GL034330.

Wang, D., C. Menz, T. Simon, C. Simmer, and C. Ohlwein, 2013: Regional dynamical downscaling with CCLM over East Asia. *Meteor. Atmos. Phys.*, **121**, 39–53, https://doi.org/10.1007/s00703-013-0250-z.

WCRP, 2009: Coordinated Regional Climate Downscaling Experiment (CORDEX). Accessed 25 March 2018, http://cordex.org/?option=com_content&view=featured&Itemid=476.

Wu, F.-T., and Coauthors, 2016: Evaluation and projection of summer extreme precipitation over East Asia in the Regional Model Inter-comparison Project. *Climate Res.*, **69**, 45–58, https://doi.org/10.3354/cr01384.

Xie, P., M. Chen, S. Yang, A. Yatagai, T. Hayasaka, Y. Fukushima, and C. Liu, 2007: A gauge-based analysis of daily precipitation over East Asia. *J. Hydrometeor.*, **8**, 607–626, https://doi.org/10.1175/JHM583.1.

Xie, Z. H., Y. J. Zeng, J. Xia, P.-H. Qin, B.-H. Jia, J. Zou, and S. Liu, 2017: Coupled modeling of land hydrology–regional climate including human carbon emission and water exploitation. *Adv. Climate Change Res.*, **8**, 68–79, https://doi.org/10.1016/j.accre.2017.05.001.

Yang, K., T. Koike, B. Ye, and L. Bastidas, 2005: Inverse analysis of the role of soil vertical heterogeneity in controlling surface soil state and energy partition. *J. Geophys. Res.*, **110**, D08101, https://doi.org/10.1029/2004JD005500.

Yatagai, A., K. Kamiguchi, O. Arakawa, A. Hamada, N. Yasutomi, and A. Kitoh, 2012: APHRODITE: Constructing a long-term

daily gridded precipitation dataset for Asia based on a dense network of rain gauges. *Bull. Amer. Meteor. Soc.*, **93**, 1401–1415, https://doi.org/10.1175/BAMS-D-11-00122.1.

Zhang, D., A. S. Zakey, X. Gao, F. Giorgi, and F. Solmon, 2009: Simulation of dust aerosol and its regional feedbacks over East Asia using a regional climate model. *Atmos. Chem. Phys.*, **9**, 1095–1110, https://doi.org/10.5194/acp-9-1095-2009.

Zhang, X., L. Alexander, G. C. Hegerl, P. Jones, A. Klein Tank, T. C. Peterson, B. Trewin, and F. W. Zwiers, 2011: Indices for monitoring changes in extremes based on daily temperature and precipitation data. *Wiley Interdiscip. Rev.: Climate Change*, **2**, 851–870, https://doi.org/10.1002/wcc.147.

Zhou, T., and R. Yu, 2005: Atmospheric water vapor transport associated with typical anomalous summer rainfall patterns in China. *J. Geophys. Res.*, **110**, D08104, https://doi.org/10.1029/2004JD005413.

Zhou, W. D., J. P. Tang, X. Y. Wang, S. Wang, X. Niu, and Y. Wang, 2016: Evaluation of regional climate simulations over the CORDEX-EA-II domain using the COSMO-CLM model. *Asia-Pac. J. Atmos. Sci.*, **52**, 107–127, https://doi.org/10.1007/s13143-016-0013-0.

Zou, L. W., and T. J. Zhou, 2013: Near future (2016–40) summer precipitation changes over China as projected by a regional climate model (RCM) under the RCP8.5 emissions scenario: Comparison between RCM downscaling and the driving GCM. *Adv. Atmos. Sci.*, **30**, 806–818, https://doi.org/10.1007/s00376-013-2209-x.

——, ——, and D. D. Peng, 2016: Dynamical downscaling of historical climate over CORDEX East Asia domain: A comparison of regional ocean–atmosphere coupled model to stand-alone RCM simulations. *J. Geophys. Res. Atmos.*, **121**, 1442–1458, https://doi.org/10.1002/2015JD023912.